Computational Studies of Nanographene Systems: Extended Discotics, Covalently Linked "Super-molecules," and Functionalized Supramolecular Assemblies

Orestis G. Ziogos,*,† Stefanos Konstantinopoulos,† Leonidas Tsetseris,‡ and Doros N. Theodorou†

†*School of Chemical Engineering, National Technical University of Athens, 9 Heroon Polytechniou Street, Zografou Campus, GR-15780 Athens, Greece*

‡*Department of Physics, National Technical University of Athens, 9 Heroon Polytechniou Street, Zografou Campus, GR-15780 Athens, Greece*

E-mail: oziogos@mail.ntua.gr

Phone: +30 210 772 3216

Abstract

Finite nanographene molecules in the form of discotic mesogens constitute a promising family of materials for a plethora of applications, primarily focused on organic electronics. Flexible side chains around the periphery of such molecules impart solubility and prompt self-organization mechanisms inherent to soft matter systems. In this work, both quantum chemical and classical simulation methodologies are employed in order to examine electronic, charge transport, structural, and dynamical properties of dis-cotic materials at multiple scales, ranging from single molecule representations to bulk supramolecular assemblies. In addition to planar molecules of variable core extent, a

series of covalently linked “super-molecules” are considered, exhibiting diverse electronic properties and low charge reorganization energies, and unique self-organization capabilities in the form of triple helix molecular wires. A hybrid Monte Carlo methodology is proposed and utilized for the creation of plausible initial configurations for atom-istic simulations in the bulk. Novel chiral supramolecular assemblies based on discotic “super-molecules” in the form of periodic molecular crystals and interfacial systems are proposed and examined with potential charge transport applications, and estimations of their charge transfer capabilities are carried out at the level of frontier molecular orbital interactions.

Introduction

Discotic molecules resembling finite graphene flakes of nanometric dimensions are currently considered as a fast evolving materials family for a plethora of applications.[1,2] An interesting feature of such molecules is their ability to host various functional groups about their periphery. The grafting of flexible side chains imparts pronounced spatial mobility to these molecules, enabling mesogens (i.e. molecules capable of producing mesophases) to self-organize into molecular wires that, in turn, are packed in a neat fashion, resulting in well-ordered molecular crystals. Due to interactions between delocalized π orbitals inherent to polyaromatic molecular structures, the most straightforward utilization of discotic materials is for organic electronics applications,[1,3] since, upon proximity of the discotic cores, charge transfer is manifested between neighboring frontier molecular orbitals via a charge hopping mechanism.[4]

Recent advances in synthesis and processing methods have led to a remarkable augmentation of the spectrum of potential applications, including materials capable of supporting both electronic and ionic conductivity[5,6] and discotics for ion storage as anode materials.[7] When coupled with polymer technology, discotic materials find applications in polymer electrolyte membranes,[8] nanographene containing polymers for organic electronics with the dis-

cotic molecules utilized either as pendant[9] or polymer backbone[10] units, and in nanoporous polymers suitable for separation processes.[11,12] Besides the utilization of discotics in their bulk, effects of nano-confinement to one-dimensional supramolecular discotic nanowires have been probed[13,14] and various applications in molecular quantum dot technology have been examined. [15–18]

Regarding theoretical work on nanographene materials, an abundance of studies across multiple simulation scales have been carried out in the literature, including ab initio and Density Functional Theory (DFT) analyses for structural and electronic properties [19–29] and charge transfer properties. [30–33] At the level of molecular wires and bulk molecular crystals, atomistic simulations[34–39] have elucidated phenomena of structural, mechanical, thermo-dynamic and dynamical nature. Furthermore, a plethora of multiscale studies[40–46] have contributed to the understanding of aspects regarding the charge transfer capabilities of discotic materials with respect to supramolecular structure and dynamics.

In a first attempt to link charge transfer to discotic core size, van de Craats and War-man,[47] based on available experimental data from molecular crystals comprised of alkyl substituted discotic molecules with core sizes ranging from triphenylene to hexabenzocoronene (HBC), proposed a conjecture predicting an increasing trend in charge mobility with respect to core size. A straightforward extrapolation postulating that larger cores would yield higher charge mobility seemed at that time plausible.[47] Nonetheless, experimental studies by Debije *et al.*[48] employing polyaromatic cores larger than HBC proved the aforementioned hypothesis incorrect. Theoretical studies have identified the root cause of charge mobility drop as being attributable to equilibrium discotic stacking patterns that diminish charge transfer rates,[42,45] albeit solubility and purification issues during material synthesis and processing are common experimental culprits.[48]

Although functionalized HBC is currently considered as the flagship discotic molecule for organic electronics applications,[1] it suffers from a serious physicochemical “ailment”: upon temperature rise, alkyl substituted HBC orthorhombic - or monoclinic, according to

the functionalization - molecular crystals melt to hexagonal liquid crystals.[49] This phase transition is followed by a radical shift in core stacking patterns that leads to charge carrier mobility drop.[48,50]

Extended polyaromatic hydrocarbons (PAHs), typically three or four times larger than HBC, form molecular crystals of hexagonal symmetry, lacking any lattice transformation upon heating,[51] thus exhibiting no abrupt conductivity variations.[48] This behavior renders them more appropriate candidates as active media for organic electronic devices when stable charge mobility over an extended temperature range is required. Furthermore, larger core molecules should exhibit superior structural robustness in the bulk, tunable barrier and mechanical properties in polymer based systems, and enhanced capacity in ion storage applications. In addition, an intriguing class of discotic materials is constituted from covalently linked PAH cores bearing dumbbell or tri-arm symmetries, [7,52–54] with variable optoelectronic properties and nano-functionality.

In this study, both quantum chemical and empirical atomistic simulations are employed in order to study electronic and charge transfer properties of discotic molecules and structural and dynamical properties of bulk molecular crystals comprised of such mesogens. Besides planar PAHs, a series of covalently linked discotic "super-molecules" are taken into consideration, at both quantum and atomistic level, with surprisingly low charge reorganization energies, elucidating the effect of molecular structure and supramolecular assembly on material properties. A unified computational approach from the level of molecular dimers to molecular wires and bulk crystals is presented, providing an "intelligent" in silico strategy for construction of plausible initial configurations which are eventually used as input for atomistic simulations. Furthermore, a hybrid class of tri-arm discotic molecules with respect to peripheral substitution is proposed, capable of exhibiting diverse molecular stacking.

The layout of this paper is as follows: Section "Computational Details" contains the description of all studied molecules, along with all necessary computational details. In Section "Results and Discussion" the results are presented and analyzed, followed by the

conclusions from this work in Section “Conclusions”.

Computational Details

Systems under study

The main focus of this work is concentrated on nanographene molecules with relatively medium molecular weight. Three key molecules are on the epicenter of our studies: HBC,[49,55] superphenalene (C96)[56] and the extended PAH of tetragonal symmetry C132.[57,58] HBC is a nanographene molecule comprised of 42 sp^2 hybridized carbon atoms with hexagonal D_{6h} symmetry. C96 is a molecule with 96 carbon atoms with trigonal shape exhibiting a D_{3h} and C132 is made up by 132 carbon atoms, bearing tetragonal C_{2v} symmetry. The two latter molecules can be envisioned as the fusion product of three and four HBC molecules, respectively. Apart from their pristine form considered in quantum mechanical calculations, all aforementioned core molecules are examined in their functionalized form as well, utilizing n-dodecyl ($C_{12}H_{26}$, C12) and phytane ($C_{20}H_{43}$, C16,4) side groups.[59,60] All nanographenes under study, along with side groups and linking peripheral sites, are illustrated in Figure 1.

Along with single PAH core molecules, a series of covalently linked “super-molecules” are also considered at quantum chemical and classical levels of description. The first kind of “super-molecule” is the dumbbell-like molecule resulting from direct covalent linkage. The rest are mesogens belonging to a multitudinous family possessing a “tri-arm” geometry, containing a series of covalent linkers that hold together three nanographene molecules. Four linking units are considered: a single nitrogen atom, a triphenylamine unit (TPA), a benzene molecule, and a triphenylbenzene (TPB) molecule. Furthermore, in the case of TPB-linked molecules, a special case of asymmetrically functionalized cores is examined where two out of three core molecules bear C16,4 side groups and the third is kept in its pristine form. HBC-based covalently linked “super-molecules” under study are depicted in Figure 2.

The idea of introducing covalent linkages between rigid, discotic molecules is not new

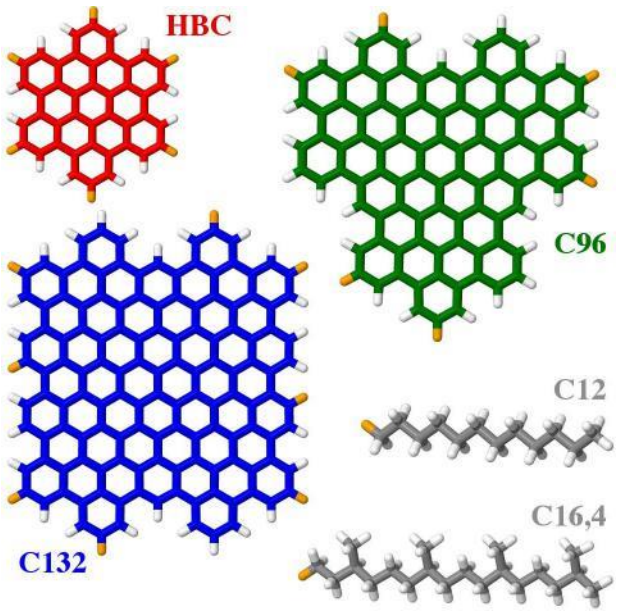

Figure 1: Molecules under study along with functionalization sites (hydrogen atoms highlighted with orange color) and flexible side chains.

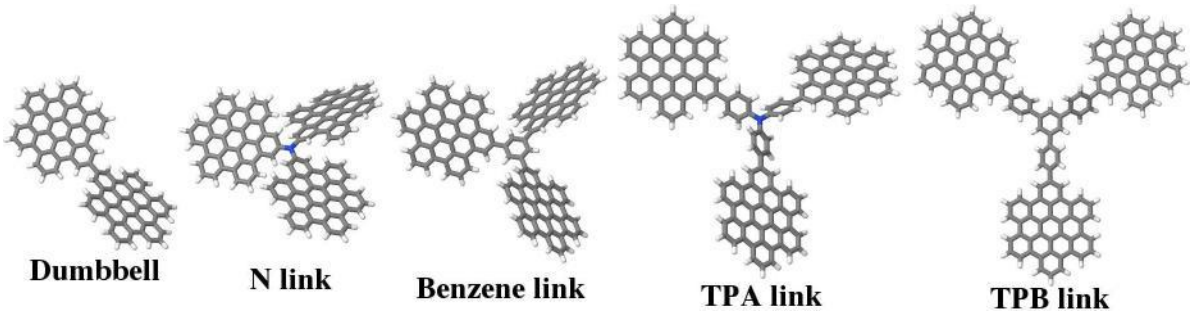

Figure 2: HBC-based “super-molecules” with different linkages.

to the literature, since both dumbbell and tri-arm geometries have been already realized for small size molecules. [61–63] Specifically for HBC, dimeric dumbbell[54] and sandwich-like[64] geometries and tri-arm geometries with nitrogen,[7] benzene[53] and TPA[52] linkers have been successfully synthesized and the utilization of TPB as bridging molecule is within experimental capabilities.[2,65–69] This fusion of discotic molecules can be viewed as a way to control polyaromatic stacking and induce structural and dynamical robustness by virtue of the physicochemical characteristics of the linking unit.

Quantum mechanical calculations

Single molecule electronic properties are evaluated at the DFT level, utilizing a 6-31G(d,p) basis set and the B3LYP hybrid functional[70,71] with dispersion corrections[72] where deemed necessary. Electron and hole reorganization energies λ are calculated from Equation 1:[73,74]

$$\lambda_{(-/+)} = E_{0(-/+)} - E_{00} + E_{0(-/+)} - E_{(-/+)(-/+)} \quad (1)$$

with E_0^0 and $E_{(-/+)}^{(-/+)}$ referring to the ground-state energies of the neutral and ionic states respectively, $E_0^{(-/+)}$ to the energy of the ionic state using the equilibrium geometry of the neutral molecule and $E_{0(-/+)}$ to the energy of the neutral state considering the equilibrium geometry of the ionic molecular state.

Charge transfer integrals (CTIs) v_{CT} are evaluated via molecular dimer calculations under the assumption that dimer molecular orbitals involved in the charge transfer process result from the interaction of monomer frontier molecular orbitals.[75] In the case of hole transport, all associated dimer matrix elements are calculated at the basis of monomer Highest Occupied Molecular Orbitals (HOMOs), whereas for electrons the calculations make use of monomer Lowest Unoccupied Molecular Orbitals (LUMOs). In the case of degenerate frontier orbitals, a root mean square average approach is adopted, taking into consideration all possible orbital combinations.[30]

All quantum mechanical calculations are carried out using the open-source software NWCHEM.[76] Charge transfer integrals are evaluated by means of the FMO-ET module embedded into NWCHEM.

Empirical Molecular Mechanics and Molecular Dynamics simulations

Molecular dimer structural optimizations are carried out for the determination of preferable stacking patterns via empirical Molecular Mechanics (MM) calculations employing two different force fields. To be more precise, for all-atom dimer simulations, the CGenFF[77,78] force field is used and for hybrid all-atom/united-atom simulations, a combination of GAFF,[79] OPLS[80,81] and GROMOS[82] force fields is utilized. Appropriate force field terms missing
from the aforementioned compilation are taken from the work of Marcon *et al.*[38] The validity of the latter hybrid force field has already been tested for functionalized HBC systems in the literature.[36,38,39]

Molecular Dynamics (MD) simulations are carried out in the isothermal-isostress statistical ensemble for bulk molecular crystals with three-dimensional periodicity and for isolated molecular wires with one-dimensional periodicity by means of the Martyna-Tobias-Klein equation of motion.[83] An integration step of 1fs is adopted and the thermostat and barostat damping constants are taken as 100 fs and 2500 fs respectively. Long range interactions are treated in the reciprocal space via PPPM mesh-based methods. [84,85] All empirical atomistic simulations are carried out using the open-source software LAMMPS.[86]

Structural and dynamical properties are calculated from equilibrium MD trajectories. The intra- and inter-columnar structure is quantified via a series of complementary methods. The most straightforward approach relies on the derivation of PAH center of mass (CoM) distance histograms. Intracolumnar molecular alignment is examined through a so-called orthogonal distance regression (ODR) line method: once PAH CoMs are calculated for each column, the ODR method returns a line that contains the CoM centroid and describes in

the most optimal fashion the spatial distribution of all columnar CoMs, defining this way a CoM director $\hat{n}_{CoM}$ for every molecular pillar.

Furthermore, specific core atoms are selected on every molecule in order to calculate two major vectors per molecule: the normal to the core vector $\hat{u}$ and the coplanar to the core vector $\hat{p}$. The orientational order tensor Q is subsequently derived for every molecular wire via Equation 2:[36]

$$Q_{\alpha\beta} = \left\langle \frac{1}{N_{col}} \sum_{i=1}^{N_{col}} \frac{3}{2} u_{\alpha}^{(i)} u_{\beta}^{(i)} - \frac{1}{2} \delta_{\alpha\beta} \right\rangle \quad (2)$$

where N_{col} is the number of molecules per column, $\delta_{\alpha\beta}$ the Kronecker delta and α and β the Cartesian indices with values x, y and z. The outer brackets symbolize a time averaging calculation scheme. The diagonalization of Q returns the orientational director $\hat{n}$, which is the eigenvector corresponding to the largest eigenvalue of Q. Strictly speaking, for tilted systems that may not exhibit perfect columnar director alignment with respect to a major Cartesian direction, the diagonalization of Q is not sufficient to determine the tilt angle of the mesogens. A safer methodology relies on the evaluation of the angle between the orientational director $\hat{n}$ and the CoM director $\hat{n}_{CoM}$ for each molecular column. Coplanar vectors $\hat{p}$ are used in order to calculate the twist angle between neighboring mesogens in pairs.

Dynamical properties are calculated via the examination of the temporal behavior of vector orientation. Regarding the orientational dynamics of normal and coplanar to molecular cores vectors, autocorrelation analyses are carried out by means of the second order Legendre polynomial of the angle formed between a vector at a specific instance and the same vector after a finite time lag t, as is expressed by Equation 3:

$$P_2(t) = \frac{3}{2}\left(\cos^2\omega(t)\right) - \frac{1}{2} \quad (3)$$

where ω is the angle formed between a vector and itself after time t and with the brackets corresponding to an average over the same vector types. In order to achieve a high accu-

racy towards the description of all dynamical properties under study, a multiple time origin calculation scheme is utilized for all vector correlation functions.

Generation of initial configurations

A challenging aspect of computational studies of soft matter systems is the construction of realistic initial configurations for atomistic simulations. In order to address this issue, all flexible side groups protruding from discotic columnar assemblies, either in the bulk or in isolated wires with one-dimensional periodicity, are grown following a bond-by-bond Monte Carlo growth scheme,[87] combined with geometry optimizations for the alleviation of unwanted atomic overlaps. A key factor inherent to the growth mechanism of linear oligomeric molecular segments involves backbone conformational statistics. Once the statistical profile of backbone proper dihedral angles is defined by means of a probability density function (PDF) $\rho(\phi_i)$, the growth procedure selects a predefined number of candidate dihedral angles N_{trial} weighted according to the a-priori PDF. Out of all trial growth moves, we select one with a probability given by Equation 4

$$p(\phi_i) = \frac{w(\phi_i)}{\sum_{j=1}^{N_{trial}} w(\phi_j)} \quad (4)$$

where $w(\phi_i)$ is the Boltzmann weight for an i-th growth move:

$$w(\phi_i) = \rho(\phi_i) \exp(-\Delta U/(k_B T)) \quad (5)$$

In Equation 5, ΔU stands for the non-bonded energy difference between the trial growth move and the previous to the growth step state and T the temperature at which the MC growth scheme is attempted.

For the growth of C12 and C16,4 side groups, an 80% *trans* [88] backbone dihedral angle profile is selected. The computational growth procedure is carried out by in-house soft-

ware, utilizing generic all-atom force fields[89,90] with full atomistic detail. The results of the bond-by-bond building process were validated for C12 melts, for which the original *trans* ratio imposed during the growth procedure was conserved. From a structural point of view, our building procedure for C12 systems reproduces the reported end-to-end distance of approximately 1.23 nm at room temperature. [88] Explicit hydrogen configurations are subsequently mapped onto a well-tested for discotic systems hybrid united-atom/all-atom representation[36,39] via the unification of aliphatic hydrogen atoms with their first neighboring sp^3 carbon atoms.

Results and Discussion

Single molecule electronic properties

As far as single molecule electronic properties of unsubstituted HBC, C96 and C132 are concerned, the expanse of the polyaromatic core affects both the relative positions of the HOMO and LUMO levels, along with the associated gap. The aforementioned energy levels accompanied by graphical depictions of frontier molecular orbitals (FMOs) are illustrated in Figure 3, including results regarding the coronene molecule.

From coronene to C96, both HOMO and LUMO appear doubly degenerate. This degenerate character is lifted for C132 due to the $_{C2v}$ point group characterizing this specific molecule. It should be noted that the molecular orbital morphology follows a distinctive benzoic character. The addition of extra benzoic rings leads to a decrease of both the HOMO-LUMO gap and the absolute position of LUMO levels, while HOMO levels show an increasing trend.

In the case of covalently linked HBC molecules, all of the examined linkage types result in a steady decrease to the HOMO-LUMO gap. FMOs retain a level of degeneracy in the case of benzene and TPB tri-arm linked molecules. Both HBC dumbbell and nitrogen linked tri-arm HBC molecules exhibit definitely non-degenerate HOMO and LUMO levels, while

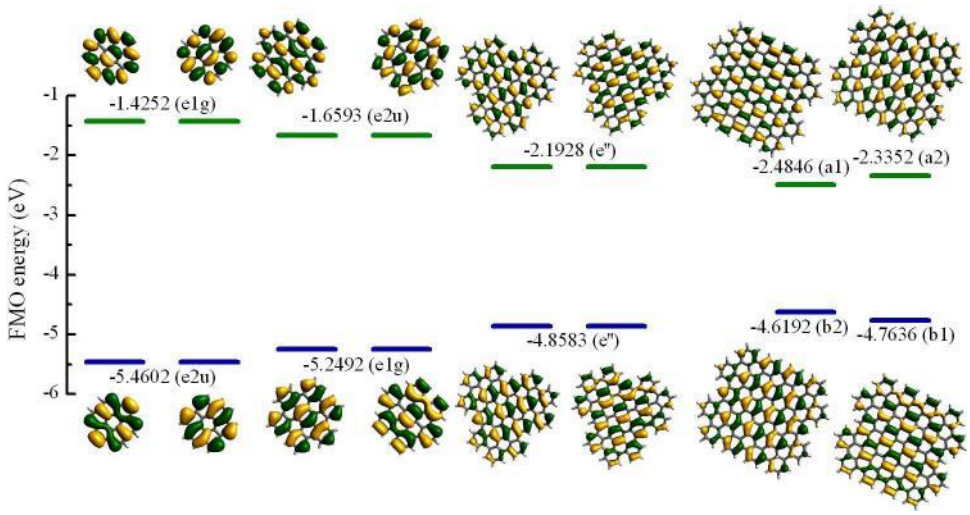

Figure 3: FMOs of coronene, HBC, C96 and C132 molecules, with associated symmetry elements inside parentheses. Occupied and unoccupied orbitals are depicted as blue and green lines, respectively.

the TPA linked tri-arm HBC molecule shows a non-degenerate HOMO and a degenerate LUMO. A graphical representation of molecular levels in the energy interval between -7.0 eV and -0.5 eV is depicted in Figure 4, including states of the HBC molecule for comparison, accompanied by illustrations of spatial distributions of FMOs. The ladder-like orbital layout in Figure 4 for states near the gap is used in order to show degenerate and near-degenerate states.

In the case of “super-molecules” that do not contain nitrogen in their linking unit, an orbital delocalization over HBC cores is evident. On the other hand, nitrogen containing molecules show a HOMO density buildup near the nitrogen atom, a characteristic inherent to the strong electron withdrawing nature of nitrogen, while LUMO levels extend around the central nitrogen atom to the HBC periphery, with a small depletion and a degeneracy lift evident for N-linked tri-arm HBC.

Upon careful investigation, the nine frontier levels near and including the HOMO of benzene and TPB linked HBC molecules appear to emanate from the HOMO(e1g), HOMO-1(e1g) and HOMO-2(a1u) states of pristine HBC. The same feature is observed for the nine

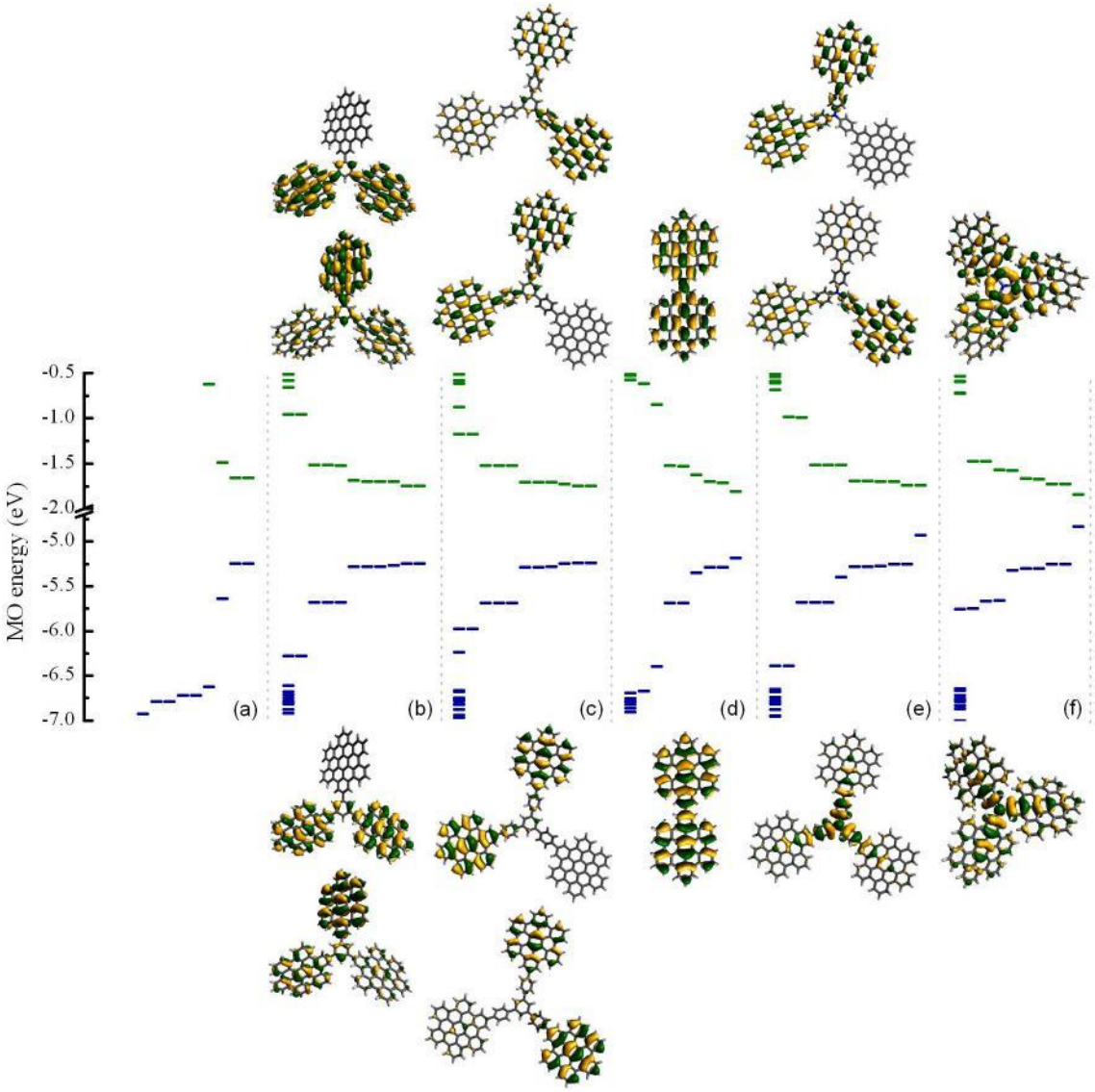

Figure 4: Molecular orbital energy levels and HOMO (bottom) and LUMO (top) illustrations of (a) HBC, (b) benzene tri-arm HBC, (c) TPB tri-arm HBC, (d) dumbbell HBC, (e) TPA tri-arm HBC and (f) N tri-arm HBC. The left to right arrangement follows the decrease in the HOMO-LUMO gap. Occupied and unoccupied orbitals are depicted as blue and green lines, respectively.

levels near and including the LUMO as well, for which the orbital manifold is comprised by the LUMO(e2u), LUMO+1(e2u) and LUMO+2(b1g) states of HBC. The benzene and TPB covalent linkers exhibit strong contributions to the electronic levels situated near -6.0 eV and -1.0 eV for the occupied and unoccupied orbitals, respectively.

Another interesting characteristic is associated with the contribution of the TPA LUMO to the unoccupied orbitals of nitrogen and TPA linked HBC molecules. In the case of nitrogen linked HBC, the LUMO mimics the spatial features of the "parent" LUMO of TPA, whereas for TPA-linked HBC, the LUMO states that appear near-degenerate are dominated by contributions from the discotic cores, with the "parent" TPA LUMO appearing near -0.6 eV. In order to rule out possible exchange-correlation functional artifacts, molecular orbital spatial distributions for the nitrogen and TPA linked HBC "super-molecules" were validated against restricted Hartree-Fock calculations that yielded the same results. Finally, the HBC dumbbell shows a typical orbital geometric layout inherent to the D_2 symmetry point group, with its FMOs constituted by HBC molecular orbitals similarly to benzene and TPB linked HBC molecules but with a two-fold degeneracy. DFT calculations regarding neutral "super-molecules" utilizing the PBE0 hybrid functional[91] were also carried out, yielding the same level of FMO degeneracy and identical orbital spatial distributions.

Absolute HOMO and LUMO levels, HOMO-LUMO gaps and electron and hole reorganization energies for all studies molecules are summarized in Table 1. Records are listed in a decreasing order with respect to the energy gap.

Given the fact that the absolute HOMO and LUMO levels of benzene and TPB are situated at -6.72 eV and 0.07 eV and -6.01 eV and -0.8 5eV, respectively, FMO energy levels of benzene- and TPB-linked HBC tri-arm "super-molecules" are dominated by the corresponding levels of HBC. This behavior is reversed for TPA-linked HBC for the HOMO, since TPA's HOMO is at -4.94 eV.

Charge carrier reorganization energies for non-nitrogen containing "super-molecules" and for all planar PAHs under study, alongside values for benzene, naphthalene and a series of

Table 1: FMO energies, HOMO-LUMO gap and reorganization energies of all molecules under study.

Molecule	HOMO (eV)	LUMO (eV)	Gap (eV)	Hole λ (meV)	Electron λ (meV)
Coronene	-5.4602	-1.4252	4.0350	130.06	171.53
HBC	-5.2492	-1.6593	3.5898	98.40	130.57
Benzene-linked tri-arm HBC	-5.2433	-1.7457	3.4976	39.88	56.77
TPB-linked tri-arm HBC	-5.2398	-1.7493	3.4905	32.93	51.31
Dumbbell HBC	-5.1810	-1.8106	3.3704	78.81	112.64
TPA-linked tri-arm HBC	-4.9281	-1.7420	3.1862	66.14	50.61
N-linked tri-arm HBC	-4.8352	-1.8441	2.9911	54.44	92.48
C96	-4.8583	-2.1929	2.6654	60.32	74.24
C132	-4.6192	-2.4846	2.1347	45.63	52.64

peri-condensed PAHs of low molecular weight (pyrene, perylene and ovalene) are plotted against the number of atoms of each molecule in Figure 5.

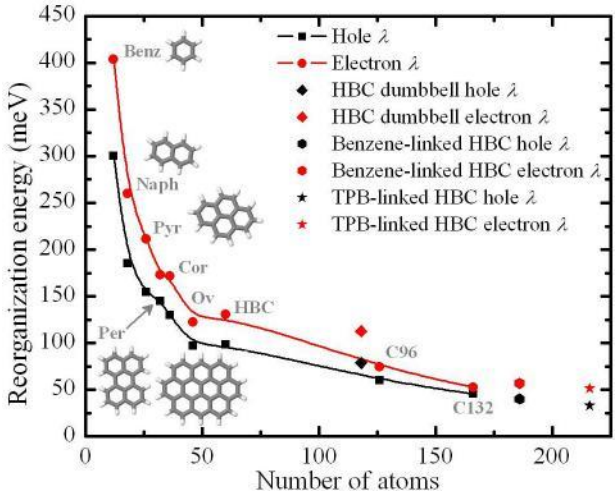

Figure 5: Electron and hole reorganization energies of planar PAHs and HBC "super-molecules" with respect to the number of atoms in every molecule. Solid lines correspond to spline interpolations on planar PAH data as a visual aid.

For planar PAHs, a decreasing trend with respect to molecular weight is evident. This general trend seems to hold even for non-planar, HBC "super-molecules". An analogous variation of hole reorganization energy with respect to the size of the molecules has been reported in the literature for small, cata-condensed PAHs.[73]

As far as the covalently linked discotics are concerned, their reorganization energies are

expected to be lying at lower levels with respect to pristine HBC, since the covalent linking in the case of the dumbbell molecule and the linking units (benzene and TPB) of tri-arm "super-molecules" facilitate a less cumbersome structural relaxation for the ionic states.

Besides the trend with respect to the core size, another interesting feature resides in the fact that all examined molecules except the TPA-linked discotic are characterized by smaller hole reorganization energies compared to electron reorganization energies, prompting such materials for p-type organic electronics applications. For TPA-linked tri-arm HBC, a marginal reversal of the aforementioned behavior is found. Analogous reorganization energy modulations via covalent linking have also been reported in the literature for TPA-substituted anthracene derivatives.[92] The utilization of articulate, aryl-based mono-substitution on TPA is found by Yang et al. to lower the $\lambda_{(+)}/\lambda_{(-)}$ ratio, without achieving a reversal similar to the one reported in this current study that makes use of rigid HBC discotic cores in a tri-arm fashion.

Molecular dimer charge transfer properties

Hole CTIs are evaluated for molecular dimers of pristine molecules under different geometrical conditions. The most straightforward analysis is linked to the dimer twist angle. Perfectly aligned molecules at a constant vertical distance of 3.6 Å are subjected to twist angle variations by rotating the upper molecule by a prescribed angle about the direction normal to the cores. The dependence of the hole transfer integral on the twist angle is shown in Figure 6.

The rotational variations for coronene and HBC are in accordance with previously published work,[42,45] although absolute values differ slightly due to the utilization of a different basis set and level of theory. It should be noted that for CTI calculations, the relatively small Gaussian basis set 6-31G is used, since larger basis sets render calculations for large molecular dimers (e.g. the ones created by C132) more demanding from a computational resources point of view.

All of the examined molecules exhibit large CTI values for graphitic-like AA stacking

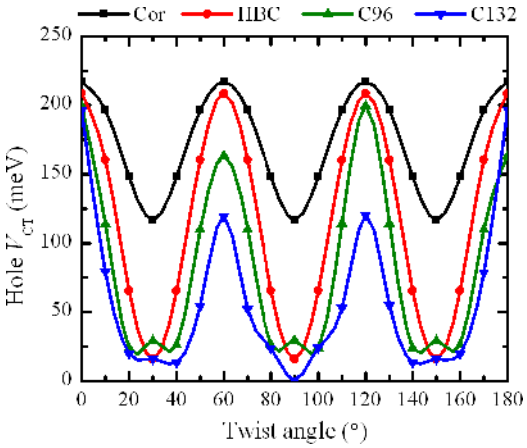

Figure 6: Evolution of the hole CTI with respect to dimer twist angle for coronene, HBC, C96 and C132.

patterns that are manifested when the twist angle is an integer multiple of 60°. Both HBC and C96 molecules show a CTI minimum threshold near 20 meV; this behavior is not observed for C132, since for a twist angle of 90° the transfer integral is effectively diminished to zero.

The next geometrical alteration to molecular dimers relies on parallel displacements along molecular high symmetry directions. For coronene, HBC and C96, parallel sliding of the top molecule by a constant step is applied along the so called armchair and zigzag graphitic directions. Due to the different edge geometry of C132, a total of four high symmetry directions are taken into consideration: two armchair and two zigzag. In Figures 7, 8, and 9, hole CTIs are plotted with respect to parallel displacements for coronene and HBC, C96, and C132 dimers, respectively. Dimer geometries that correspond to CTI maxima are also shown, with the armchair and zigzag displaced molecules depicted in black and blue colors for all molecules except C132.

All discotic molecules exhibit CTI maxima when the applied displacement manages to reproduce a graphitic AA stacking pattern or variants of the so-called AA' stacking pattern.[93] For C132 molecular dimers, AA' stacking motifs are depicted in detail in Figure 9 as insets. It should be noted that manifestations of AB-like graphitic stacking patterns do not generally yield high transfer integral values. This fact is demonstrated in Figure 9 where AB stacking

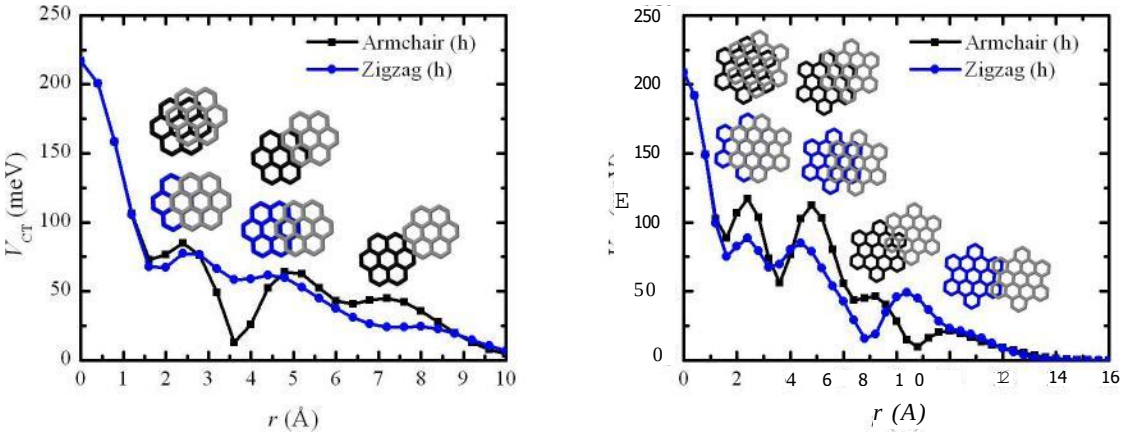

Figure 7: Evolution of the hole CTI with respect to parallel displacements for coronene and HBC.

Figure 8: Evolution of the hole CTI with respect to parallel displacements for C96.

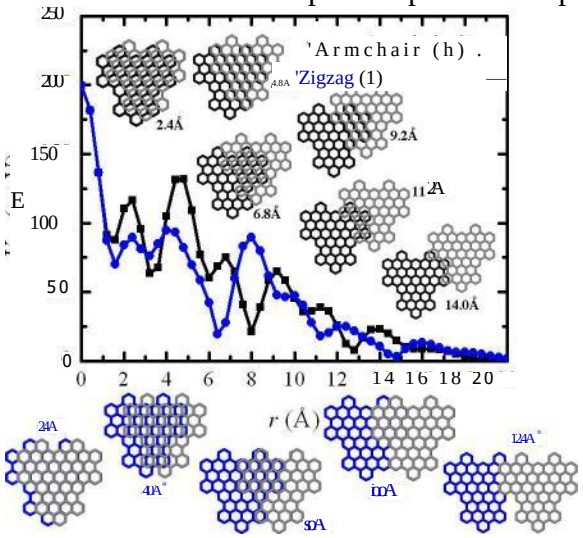

patterns arising when shifting a C132 molecule along an armchair direction are highlighted using discrete red stars.

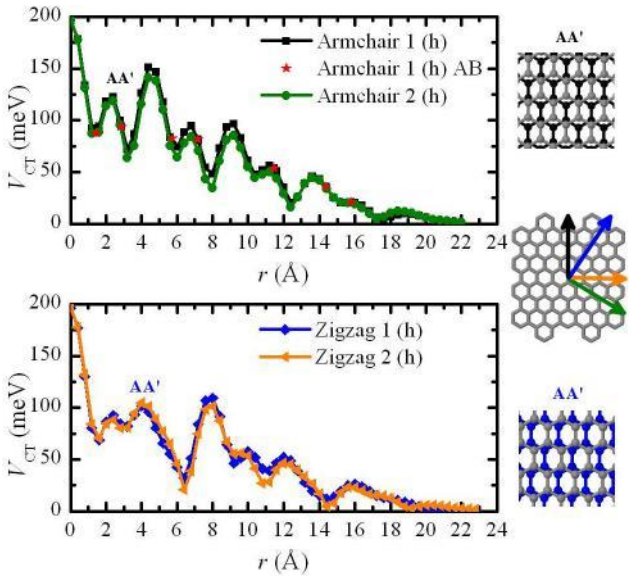

Figure 9: Evolution of the hole CTI with respect to parallel displacements for C132. The arrows indicate the different sliding directions. Red stars in the upper diagram correspond to AB stacking patterns. Selected AA' stacking patterns are also highlighted.

Interestingly enough, the sliding direction seems to affect the CTI maxima heights for small displacement values. Although this behavior is quite subtle for coronene, this is not the case for HBC, C96 and C132. These molecular dimers show more pronounced maxima along the armchair displacement direction, registering two major peaks for displacements up to 6 Å, with associated heights over 100 meV.

Stacking patterns from empirical MM

For every constructed molecular dimer, a static geometry minimization is utilized in order to obtain a relaxed structure associated with a potential energy minimum. In Figure 10 we report the dimerization energy minima evaluated for every configuration. The dimerization energy is calculated as the sum of all non-bonded intermolecular interactions. The left, middle and right diagram panels correspond to energy data for hexa-*n*-hexyl substituted HBC (HBC-C6) and C96 (C96-C6) and octa-*n*-hexyl substituted C132 (C132-C6) cores,

respectively. Furthermore, each panel contains two data categories: the ones situated on the left (black, green and cyan) correspond to the total dimerization energy of the system, while the ones situated on the right (red, blue and magenta) to the core atoms dimerization energy. This refinement was deemed necessary in order to clarify the lowest core energy states and the associated stacking patterns. In the same figure, illustrations of these low energy stacking patterns are shown for every system.

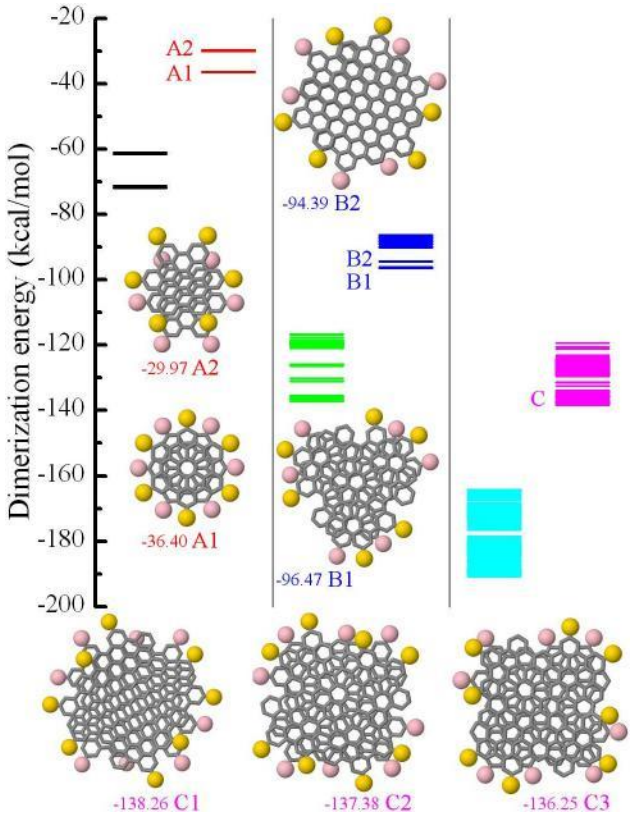

Figure 10: Dimerization energy minima and associated stacking patterns for HBC-C6 (left), C96-C6 (middle) and C132-C6 (right). In each panel, the left states register the total dimer-ization energy and the right states the core atoms dimerization energy. The pink and yellow spheres represent the linking side chain sites for the lower and upper molecule, respectively. Every low energy stacking pattern is shown alongside its core energy.

For HBC-C6, there are two core energy minima: the global minimum A1 (see Figure 10) corresponds to a daisy-like stacking pattern with a twist angle of 30° and the local minimum A2 to a parallel displaced dimer configuration. The lowest energy structural results are in agreement with quantum mechanical findings from the literature[19] while the geometry of the

A2 minimum is similar to the stacking pattern proposed by experimentalists for crystalline HBC-C12[94] and recently identified as the metastable AA' graphitic stacking pattern.[93]

In addition, to support the validity of the utilized hybrid force field, the same dimer calculations were carried out using the CGenFF[77,78] force field with explicit hydrogen atoms. The minimum energy structures obtained coincide with the ones reached via the simpler force field, reinforcing confidence in its predictive power.

As far as the stacking patterns of the other two mesogens are concerned, C96-C6 exhibits two refined minima: the global minimum B1 that is inherent to a daisy-like stacking pattern of a 20° twist angle and the local minimum B2 which corresponds to a graphitic AA stacking resulting after a 60° core rotation. For C132-C6, the stacking energetics appear more complicated, even after the core atoms energy refinement. This system exhibits a wide low energy states band (labeled C in Figure 10). Upon careful inspection, this band supports three dominant stacking patterns: a graphitic-like pattern C1 that results after a 60° twist angle, and two daisy-like patterns, C2 and C3, with a twist angle of 20° and 90° respectively, all listed in ascending order with respect to the core atoms dimerization energy.

MD simulations of molecular wires

Information regarding minimum energy stacking patterns for C96 and C132 PAHs is used in order to create molecular wires with plausible internal stacking substructure. In the case of C96-based systems, the existence of minima B1 (20° twist angle) and B2 (60° twist angle) prompts the utilization of three symmetric stacking motifs: a 60° twist angle profile that corresponds to a graphitic-like AA stacking, an alternating 20° twist angle profile and a helical 20° twist angle stacking profile. Once the internal molecular wire structure is determined, side chains are created using a MC growth scheme and the resulting systems are equilibrated via MD simulations. An interesting characteristic of non-chiral dodecyl substituted C96 molecular wires is the transition to the helical 20° twist angle stacking profile upon heating at 400 K. Twist angle time series of a periodic C96-C12 molecular

wire initialized with a graphitic stacking pattern are shown in Figure 11 alongside molecular representations of the initial and final structures with lifted periodic boundary conditions for clarity. In the molecular depictions in Figures 11 and 12, bulky green spheres correspond to aromatic linking carbon atoms where side chains are grafted, blue graphical elements are assigned to aliphatic -CH_2- units and the red ones to terminal -CH_3 units.

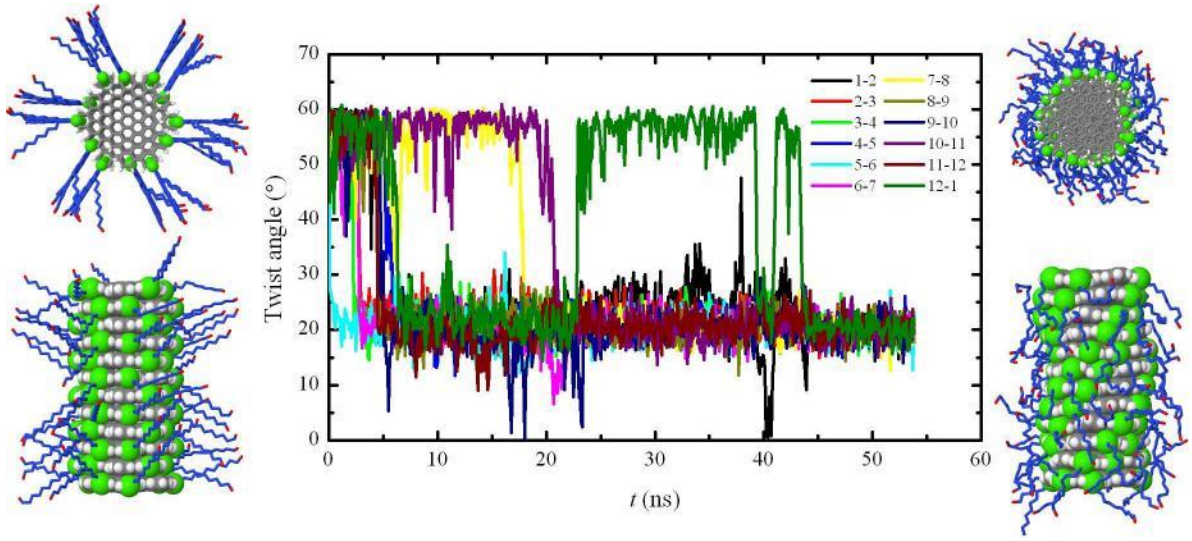

Figure 11: Twist angle time series at 400 K of a periodic C96-C12 molecular wire comprised of twelve molecules and initialized to a graphitic-like stacking pattern. Molecular representations on the left and on the right side of the diagram correspond to top and side views of the initial and final states, respectively.

The utilization of heavier and bulkier C16,4 side chains decelerates the transition between different stacking patterns. To overcome this obstacle, MD simulations at higher temperatures were employed. During these simulations, the 60° stacking pattern gradually transforms to patterns with 20° twist angle, with the temperature rise expediting the transition. Similarly to C96-C12 molecular wires, the most stable stacking pattern arising from MD simulations is the chiral arrangement with a 20° twist angle.

In the case of C132 cores, the three low energy stacking patterns of 20°, 60° (graphitic) and 90° twist angle identified via MM dimer calculations lead to five molecular wire stacking profiles. Four of them correspond to alternating and helical arrangement bearing 20° and 60° twist angles, while the fifth is constructed considering a 90° twist angle. It should be

noted that the 2-fold symmetry of C132 can support a 60° helical motif, as opposed to C96 where the 3-fold molecular symmetry cannot discriminate between a possible alternating or chiral nature for the 60° twist angle stacking pattern.

Simulations of C132-C16,4 molecular wires exhibit a slower temporal evolution due to augmented molecular weight of the mesogens. Graphitic stacking patterns with both alternating and helical arrangements transform at elevated temperatures to mixed stacking patterns with both 20° and 90° twist angle stacking patterns. Twist angle time series and molecular snapshots for a chiral 60° C132-C16,4 periodic nanowire with initial graphitic arrangement are depicted in Figure 12.

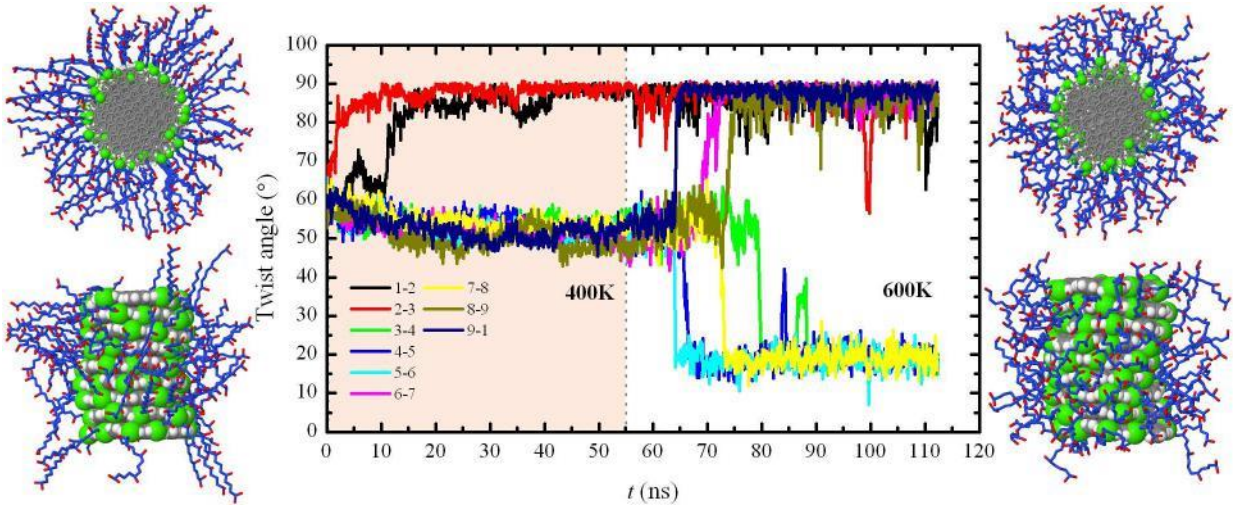

Figure 12: Twist angle time series at 400K and 600K of a periodic C132-C16,4 molecular wire comprised by nine molecules and initialized to a graphitic-like stacking pattern. Molecular representations on the left and on the right side of the diagram correspond to top and side views of the initial and final states respectively.

From the initial five stacking configurations examined for C132-C16,4 molecular wires, both alternating and helical graphitic-like profiles were found metastable, since transitions to mixed 20°/90° stacking profiles were manifested upon sufficient temperature rise. On the other hand, both alternating and helical 20° patterns and the 90° twist angle stacking pattern remain structurally invariant.

Based on all aforementioned findings, for bulk simulations we choose to examine pristine

helices of 20° twist angle for C96-based systems and four different stacking variants for C132-C16,4: the alternating 20° and 90° profiles, the helical 20° profile and the mixed 20°/90° stacking motif.

MD simulations of bulk molecular crystals

Periodic molecular crystals comprised of grafted discotic molecules with intracolumnar structure in accordance to single column simulations findings are generated via the application of the previously outlined MC growth methodology. Initially, nanographene pillars of stacked pristine PAH molecules with predefined twist angle profiles are placed on a two dimensional hexagonal lattice, with lattice constants taken from experimental data. [60] The aliphatic nanophase is subsequently grown, avoiding this way any possible structural artifacts that could arise should pre-grown isolated molecular wires be brought into proximity for the creation of the molecular crystal.

All bulk systems are made up of sixteen supramolecular columns, with each column bearing a variable number of molecules in order to adhere to the applied periodic conditions. In particular, HBC- and C96-based molecular crystals contain twelve molecules per column. C132-based systems with alternating 20° and 90° twist angle have ten molecules in each column and the remaining chiral system with a twist angle of 20° and the mixed 20°/90° stacking system have both nine molecules in every molecular pillar. Molecular crystals are equilibrated via MD simulations in the isothermal-isostress statistical ensemble at six different temperatures, ranging from 300 K to 400 K with an interval of 20 K. Triclinic periodic simulation boxes are utilized, with an anisotropic barostat maintaining the pressure at 1 atm.

Systems under study retain the two dimensional hexagonal symmetry of the columnar lattice in the examined temperature range. Molecular pillars remain highly ordered, since orientational order parameter studies on both CoM directors and perpendicular core vectors yield upon diagonalization single maximum eigenvalues above 0.99, indicating strong align-

ment. For all cases, CoM directors are practically aligned with the (0,0,1) vector in space. Furthermore, initial twist angle profiles remain unaffected, except in the case of C132-C16,4 molecular crystals with alternating 20° profile, for which twist angles are slightly shifted to approximately 17°.

Structural information regarding distances between molecular pillar and core-to-core distances inside each column can be extracted from CoM distance histograms $h(r)$. For the calculation of intercolumnar distances, an alternative approach is also considered: besides typical distances between core CoMs, a more elaborate method is utilized that results in vertical intercolumnar distances. To be more precise, should a specific molecular column be taken into consideration, we calculate the perpendicular distance of each CoM belonging to this column from the ODR lines of neighboring columns. Both $h(r)$ and vertical CoM distance from neighboring ODR lines histograms $h_{\perp}(r)$ are depicted in Figure 13 for all examined molecular crystals at 400 K. The dotted gray lines correspond to available experimental data regarding intercolumnar distances. [60] The inset graph for HBC-C16,4 shows all peaks compliant to the hexagonal symmetry, including peak position ratios. Small distance peaks of the C96-C12 system are eclipsed by the peaks of the C96-C16,4 system.

The effect of temperature rise on selected structural properties is outlined in Table 2, where two basic parameters are included in the form of a dyad containing the intercolumnar distance calculated using the vertical CoM distance from the neighboring ODR lines method and the molecular tilt separated by a slash.

As far as the hexagonal lattice constants and the core tilt are concerned, a general trend is evident for all molecular crystals examined except the C132-C16,4(20° alt) system: the rise in temperature leads to positive thermal expansion accompanied by a tilt reduction. A characteristic example of the effect of the stacking pattern on the structure of such materials is found in the excluded system. The alternating 20° stacking profile for C132-C16,4 results in relatively highly tilted systems that exhibit an out of the ordinary response to temperature rise: the core-to-core distance decreases upon heating, the tilt angle follows an

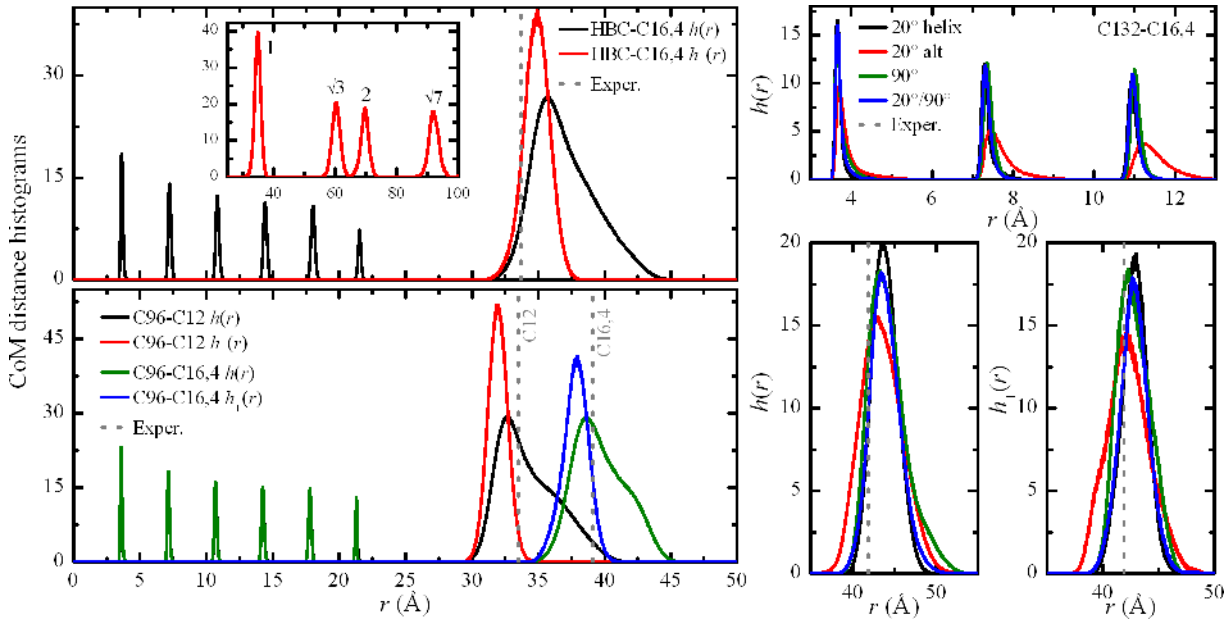

Figure 13: Molecular core CoM distance histograms h(r) alongside vertical CoM distance from neighboring ODR lines histograms h⊥(r) for functionalized discotic molecules in the bulk at 400 K.

Table 2: Intercolumnar distances (expressed in Å) and core tilt angles with respect to temperature for systems (each system's twist angle profile is noted inside parentheses): a. HBC-C16,4(30°), b. C96-C16(20°), c. C96-C16,4(20°), d. C132-C16,4(20°), e. C132-C16,4(20°alt), f. C132-C16,4(90°alt), g. C132-C16,4(mixed 20°/90°).

ID	T (K)					
	300	320	340	360	380	400
a.	34.08/2.36°	34.38/1.72°	34.42/1.64°	34.49/1.56°	34.60/1.35°	34.88/1.12°
b.	31.47/1.68°	31.56/1.72°	31.60/1.43°	31.76/0.72°	31.90/0.41°	31.94/0.56°
c.	37.07/2.56°	37.14/2.68°	37.32/2.12°	37.38/1.43°	37.82/1.76°	37.87/1.41°
d.	41.91/3.56°	42.22/4.48°	42.25/4.70°	42.46/3.84°	42.43/4.27°	42.87/4.58°
e.	42.23/6.87°	42.43/7.90°	42.53/11.06°	42.50/11.20°	42.44/13.75°	42.18/17.46°
f.	42.04/5.65°	42.19/4.27°	42.20/5.15°	42.41/4.31°	42.34/4.22°	42.62/3.57°
g.	42.44/3.67°	41.75/3.01°	42.26/3.23°	42.39/3.93°	42.60/3.42°	42.79/3.04°

increasing trend and the lateral with respect to the columnar direction lattice expansion shows a maximum, resulting in a molecular crystal with smaller lattice constants at 400 K in comparison to the room temperature analogue. A similar negative thermal expansion manifestation has already been pointed out in the literature via experimental[95] and theoret-ical[39] investigations of discotic materials. It should be noted that tilted C132-C16,4(20° alt) molecular crystals lack any specific tilt motif like the "herringbone" tilt pattern inherent to HBC derivatives. [36,39]

In the case of the side chain *trans* population upon heating, all phytyl substituted systems converge approximately to a 64% *trans* population, while the dodecyl substituted C96 molecular crystal shows a clear decrease towards near 58%. This difference is expected, since the pendant methyl groups of C16,4 should relatively hinder side chain coiling. It should be noted that the original 80% *trans* population is not conserved by any studied system, indicating that the aliphatic nanophase is equilibrated to a state where the side chains are not overextended towards an *all-trans* configuration, characteristic of highly crystalline systems.

The effect of temperature on core dynamics is examined via vector autocorrelation function (ACF) analyses through second order Legendre polynomial orientational correlation measurements. Two basic core vectors are considered: a normal to the PAH core and a coplanar one. Selected ACFs are depicted in Figure 14.

According to vector ACF analyses, the rise in temperature leads to increased core mobility. Nevertheless, ACF curves exhibit a saturative behavior towards hard plateaus situated above 0.985 and 0.970 for normal and coplanar vectors, respectively. The effect of different substitution is depicted in Figure 14 for C96-based molecular crystals where the mesophase plateaus are drawn with dotted lines, leading to the conclusion that lighter C12 side chains lead to more pronounced thermal motion, retaining, however, the saturative behavior. Poly-morphs of C132-C16,4 show similar vector dynamical response to C132-C16,4(20°), indicating that the stacking pattern has a minuscule effect.

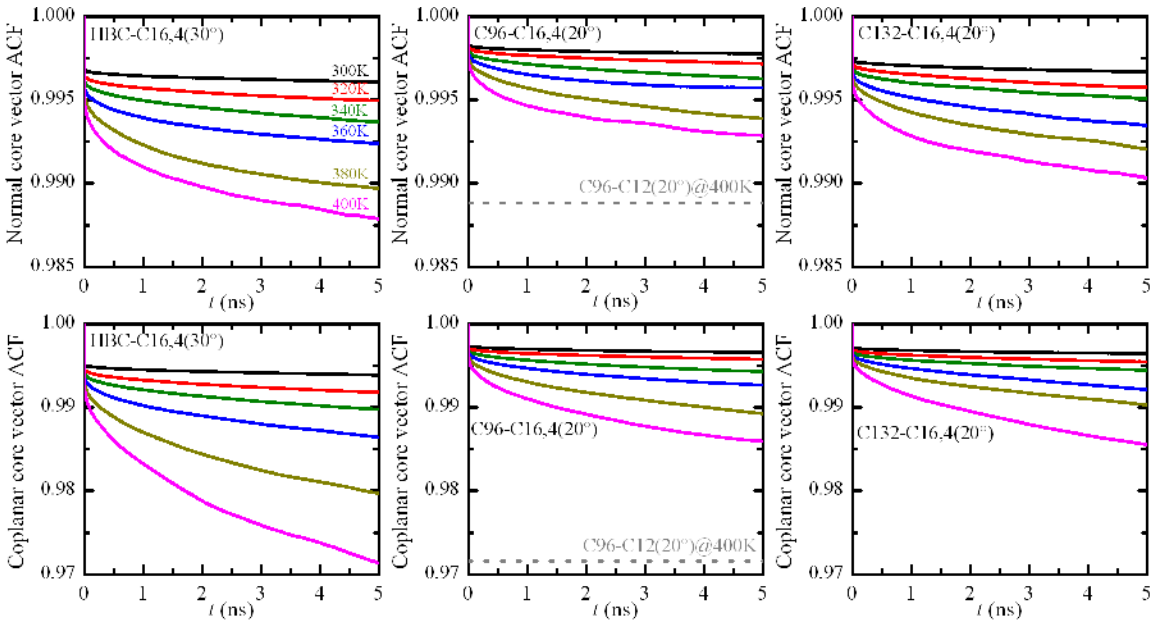

Figure 14: Autocorrelation spectra of the normal and coplanar to the PAH core vectors. The temperature color labeling of the upper left diagram applies to all others. Dashed lines correspond to C96-C12 plateaus at 400 K.

Supramolecular assemblies of discotic “super-molecules”

Isolated molecular wires and molecular crystals comprised of functionalized “super-molecules” with tri-arm symmetry and TPB linkage are examined via MD simulations, utilizing HBC, C96 and C132 cores. The role of the linking TPB unit is evident: the non-coplanar arrangement of the outer phenyl rings with respect to the inner ring prompts the attached discotic molecules to align parallel to the plane of the inner phenyl ring. This planar configuration cannot be achieved with stiffer, less articulated linking units, like a nitrogen atom or a single phenyl ring, since such linkanges form propeller-like geometries due to steric hindrance. As far as the peripheral substitution is concerned, all molecules are functionalized with phytyl side chains through the introduction of two distinct grafting variants. The first variant relies on symmetric substitution, with every discotic sub-unit bearing the same number of side chains, while the second on an asymmetric substitution scheme that leaves a discotic molecular fragment in its pristine, unsubstituted form.

For the description of the overall orientation of stacked “super-molecules”, the notion

of the linkage twist angle is introduced. For tri-arm geometries with TPB linking units, the vector that connects the geometric centers of the inner and a predefined external TPB phenyl ring is used for the calculation of the linkage twist angle between neighboring “super-molecules”. Having in mind the definition of the linkage twist angle, a series of single column initial configurations with different linkage twist angles of 0° (cofacial alignment) and 10°, 20° and 30° are generated and equilibrated via MD simulations.

In order to comprehend the structure of the examined tri-arm supramolecular pillars, two characteristic molecular wires made up of symmetrically and asymmetrically substituted TPB-linked C132 “super-molecules” are depicted in Figure 15, alongside single molecule representations. The blue spheres correspond to side chain -CH_2- units and the red spheres to pendant and terminal -CH_3 units. Inner discotic carbon atoms are colored grey, outer linking atoms to which side chains are grafted are depicted with enlarged green spheres and sp^2 hybridized carbon atoms bearing hydrogen atoms on the core periphery are colored orange. Finally, TPB carbon atoms linked only to other carbon atoms are shown using pink spheres. For both molecular wires in Figure 15, a three-stage rendering is chosen: the first stage utilizes all simulation atoms, showing this way the surrounding aliphatic mantle; the second stage depicts only core atoms, while the third reduces core atoms from spheres to sticks in order to show the inner structure of the TPB supramolecular cord.

For all tri-arm single column systems under study, the lowest energy corresponds to chiral configurations with a linkage twist angle of 10°. Having this information at hand, periodic molecular crystals in compliance with the aforementioned supramolecular stacking profile are created by placing unsubstituted molecular pillars on a hexagonal lattice of predefined spacing and subsequently growing the aliphatic nanophase utilizing the hybrid MC growth method.

As far as the substitution scheme is concerned, symmetrically substituted systems of HBC, C96 and C132 cores bear three, four and six phytyl side chains per discotic unit. The initial substitution scheme relied on the convention to use as many side chains per core as

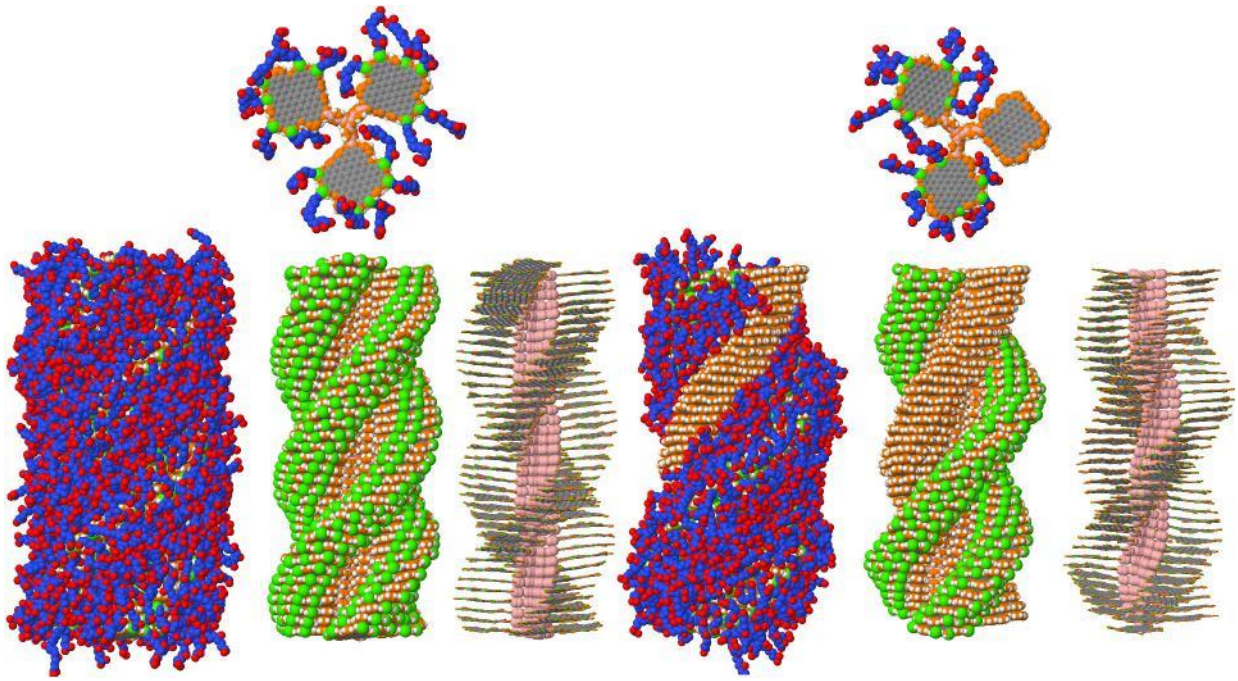

Figure 15: Single molecule representations of symmetrically (top left) and asymmetrically (top right) substituted TPB-linked C132 “super-molecules”. The bottom depictions constitute three-stage renderings of molecular wires with a chiral 10° linkage twist angle profile.

were utilized for non-linked systems minus two. This way, one grafting site is reserved for the TPB linker and its nearest site is ignored in order to minimize the probability of TPB cord perforation by the side chains. This scheme leads to nicely stacked TPB-linked C96 and C132 systems but not for HBC-based pillars, since the utilization of four side chains per core resulted in severe side chain penetration into the TPB cord during the MC side chain growth step. For this reason, the number of three side chains per core is chosen for TPB-linked HBC systems. In the case of asymmetrically substituted tri-arm “super-molecules”, for HBC-based systems the same number of side chains per disk is maintained, whereas for C96- and C132-based systems the maximum number of five and seven functional groups per core is chosen in order to enhance their potential solubility.

After the creation of the side chain nanophase, all systems are equilibrated via MD simulations at 400 K utilizing triclinic periodic supercells. Symmetrically substituted molecular crystals exhibit lateral hexagonal lattice constants of 46.4 Å, 58.3 Å and 66.5 Å for HBC,

C96 and C132 tri-arm systems respectively and the vertical distance along the stacking direction of TPB CoM is near 3.7 Å for all studied molecular crystals. The linkage twist angle exhibits a unique maximum situated at 10°. As far as discotic core structural features are concerned, the tilt angle with respect to TPB cord directors is found at 4.5°, 5.5° and 9.0° for HBC-, C96- and C132-based systems. Another angular quantity measured from equilibrated MD trajectories is the pitch angle of each protruding disk in reference to the TPB cord director. Calculated pitch angles are situated slightly above 90° for all molecular crystals. Core mobility is also quantified via normal and coplanar vector orientational ACF functions. Characteristic results for both symmetrically and asymmetrically substituted C132-based tri-arm systems are shown in Figures 16 and 17. HBC- and C96-based tri-arm systems exhibit analogous properties.

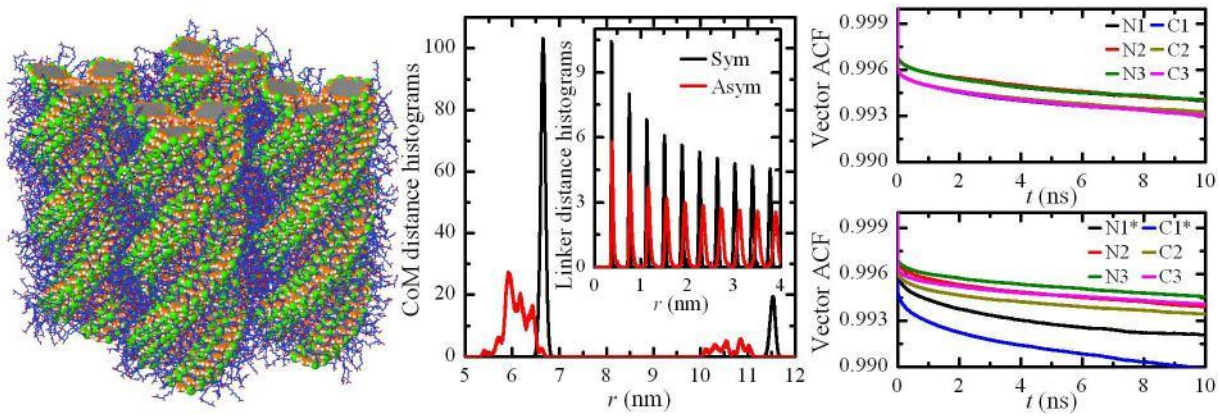

Figure 16: Graphical depiction of a molecular crystal of symmetrically substituted TPB-linked C132 “super-molecules” with lifted periodic boundary conditions (left panel), CoM distance histograms (central panel) and normal (N) and coplanar (C) vector orientational ACF functions (right panel) with respect to the substitution scheme.

The effect of the substitution scheme shows a rather counterintuitive behavior. One would suspect that the lack of side chains on one of the three linked discotic cores should lead to more pronounced structural and dynamical order, since in the asymmetrically substituted systems, the entropic contributions are reduced in comparison to fully substituted molecules. Analyses at equilibrium indicate that the exact opposite phenomenon takes place: the partial absence of grafted side chains results in structural disorder and more pronounced disk

mobility, indicating that the amorphous side chain nanophase acts as a stabilizing medium for such systems.

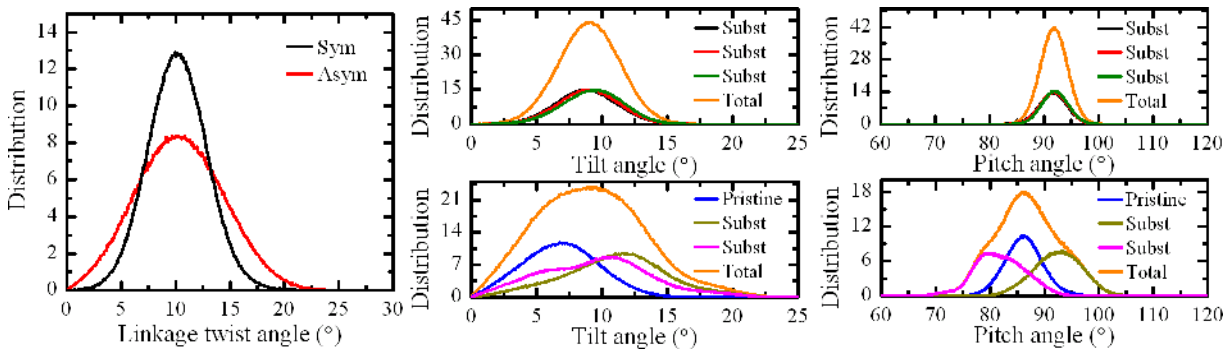

Figure 17: Angular quantities characteristic of the intracolumnar structure for the TPB-linked C132 molecular crystal with respect to the substitution scheme.

Upon careful inspection of the structural quantities plotted in Figures 16 and 17, the induced asymmetry to the substitution scheme leads to smaller intercolumnar distances and to discrepancies in core tilt and pitch angles. Furthermore, dynamical studies indicate that pristine cores (N1* and C1* in the right panel of Figure 16) are more mobile compared to substituted cores, a behavior showing that tangential core interactions are not adequate to stabilize discotic movement. Should all aforementioned findings be taken into consideration, the role of the soft, amorphous aliphatic nanophase is to be revised: instead of attributing only entropic characteristics to the side chain mantle, one needs to also consider this very nanophase as a stabilizing agent with “gluing” properties with respect to structural and dynamical uniformity.

Symmetrically substituted C96- and C132-based tri-arm bulk molecular crystals are also examined with respect to the manifested discotic stacking patterns inside each three-fold chiral molecular pillar. To this end, a more intricate method for the determination of stacking profiles is utilized, since a simple core twist angle analysis cannot be applied due to the fact that discotic CoMs are out of alignment. Discotic segments are examined into dimeric first neighboring dyads. For each dyad, the lower core CoM is considered as the origin of a local two-dimensional coordinates system. In this system of coordinates, the vertical projection

of the position of the upper CoM is recorded, alongside the dimer core twist angle. By applying a binning procedure with respect to twist angles, two-dimensional distributions of upper CoM projections are accumulated. For all examined systems and twist angle bins, CoM projection contours exhibit a unimodal nature, enabling thus a straightforward determination of statistically significant stacking patterns derived from MD trajectories. The population of the dominant stacking pattern with respect to the core twist angle for tri-arm C96 and C132 molecular crystals is shown in Figure 18. Inset dimer depictions correspond to most probable stacking patterns, with the violet spheres indicating the PAH carbon atom connected to the TPB covalent linker.

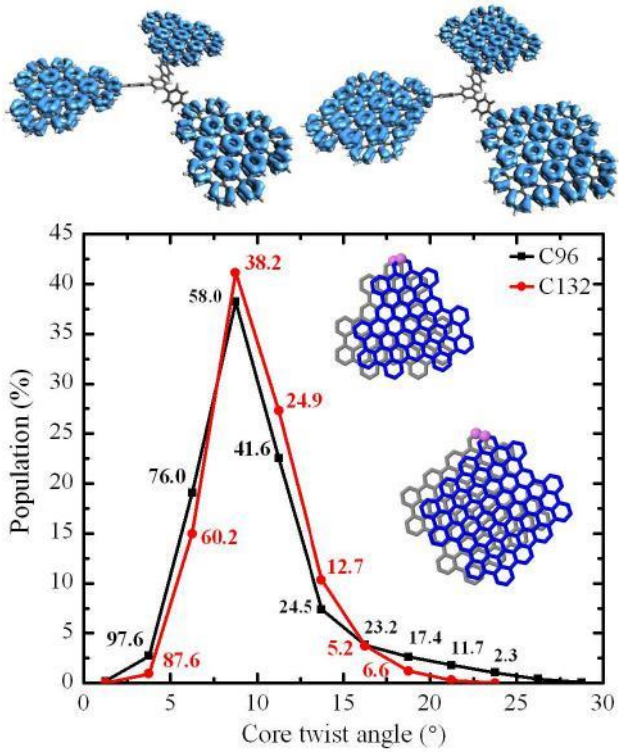

Figure 18: Partial electronic density contour plots near the HOMO state of TPB-linked C96 and C132 molecules (top) and the statistical distribution of dominant stacking patterns with discrete core twist angle (bottom). The numbers next to statistically significant points correspond to CTI values (expressed in meV) for hole transfer and the inset depictions correspond to the most probable dimer stacking patterns.

The stacking pattern statistical analysis can be utilized in order to extract valuable information regarding charge transfer properties. DFT calculations on single tri-arm molecules

on the B3LYP-D3/6-31G(d,p) level of theory show that the electronic density attributed to states from the HOMO-8 to the HOMO level is localized on the discotic segments. Having this information at hand, a first approach for hole transport CTI calculations can be established on the basis of the HOMO and HOMO-1 levels, in full analogy with the case of isolated dimers. All calculated values are listed in Figure 18 next to each stacking pattern point. A decreasing trend with respect to the core twist angle is evident for hole CTI values. Nevertheless, the values of most probable stacking profiles indicate the suitability of such supramolecular chiral structures for charge transfer applications. For C132-based tri-arm geometries in particular, the utilization of the TPB linker prohibits C132 discotic cores from forming 90° stacking patterns, thus improving the potential charge transfer mechanism.

Although asymmetrically substituted "super-molecules" failed as more structurally robust bulk candidates, their application as cofacially stacked molecular monolayers is found to be quite promising. To this end, an interfacial system of cofacial TPB-linked C132 tri-arm molecules with asymmetric phytyl substitution is created by placing the monolayer on top of a silicon substrate. A characteristic depiction of such a prototype system is shown in Figure 19.

In this interfacial arrangement, substituted C132 discotic cores adopt the typical stacking profile with core twist angles near 20°. On the other hand, pristine segments exhibit near-graphitic stacking patterns, with core twist angle values limited below 10°. A selection of statistically significant stacking motifs of unsubstituted cores is depicted in Figure 19, together with their associated hole CTI values. The aforementioned values constitute this type of self-organization appealing for charge transfer applications. Furthermore, the exposed pristine graphitic segments can - in principle - serve as nanopatterned intercalation arrays for either hydrogen or ion storage and as firmly aligned nanographene edges for a plethora of applications.

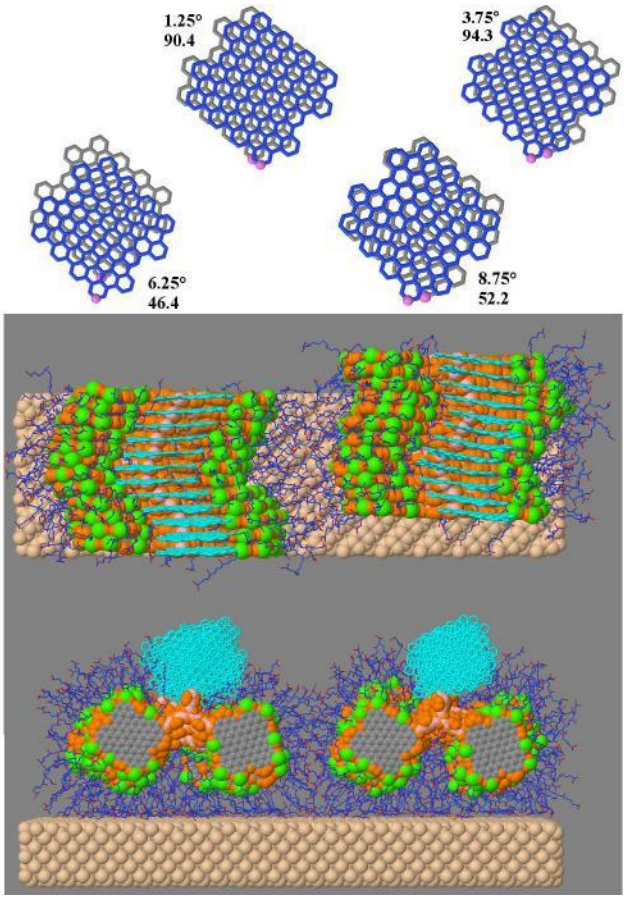

Figure 19: Graphical depiction of an interfacial system comprised by a cofacially aligned monolayer of asymmetrically substituted TPB-linked C132 molecules on top of a silicon substrate. Hydrogens are omitted for clarity. Dominant stacking patterns of pristine C132 cores (colored cyan in the slab representation) are also shown, alongside core twist angle and hole CTI values in meV.

Conclusions

Single molecule DFT studies elucidate the effect of discotic core size of planar PAHs on electronic and charge transport properties, with the HOMO-LUMO gap and reorganization energies decreasing as the core size is extended. In the case of discotic “super-molecules”, covalent linking of HBC molecules has been proven to be an effective way to tune the gap between the values of HBC and C96, also altering the level of degeneracy in the case of the HBC dumbbell and nitrogen containing linkers. As far as hole and electron reorganization energies are concerned, a monotonic decrease with respect to the number of atoms is found. Moreover, the utilization of articulate covalent linkers is proven to be a promising molecular alteration in order to reduce reorganization energies.

At the molecular dimer level, quantum chemical calculations of CTIs with respect to core twist angle exhibit maxima at graphitic-like stacking. For the C132 mesogen, a global minimum at a twist angle of 90° at which CTI drops to zero is identified, exposing a highly “unwanted” dimer configuration for charge transport calculations. Studies based on parallel displacements along high symmetry directions return non-zero CTI values even for dimer configurations with minimum overlap and pronounced maxima at AA and AA’ stacking patterns in the case of significant geometric overlap.

A hierarchical approach for the creation of initial configurations from the level of a molecular dimer to an isolated molecular wire and to a molecular crystal is proposed and utilized in the case of alkyl substituted discotic molecules. The methodology relies on predicting favourable stacking patterns at the dimer level using empirical force fields; creating single column systems according to findings from dimer calculations; and studying the energetic and the evolution of the structural features using MD simulations. Results from single column simulations are used in order to select energetically more favourable structures to create molecular crystals.

Molecular crystal creation for systems with disordered alkyl nanophase is based on a hybrid MC growth scheme that minimizes artifacts due to side chain collapse should equili-

brated single columns be used. Structural studies on functionalized HBC-, C96- and C132-based molecular crystals suggest that these particular mesogens form robust bulk assemblies at the examined temperature range from 300 K to 400 K. In particular for C96-C12 and C96-C16,4, a chiral stacking pattern with a core twist angle of 20° is proposed, in fine agreement with experimental structural findings. For C132-C16,4 molecular crystals, four polymorphs are examined with various stacking motifs. Graphitic-like stacking patterns have been proven not to be preferable. Furthermore, the manifestation of 90° twist angle stacking patterns is plausible for this system, thus hindering its charge transport capabilities due to extremely low CTI values associated with this stacking motif. In addition, should an alternating 20° twist angle pattern be adopted, this particular arrangement results in molecular crystals with finite tilt with respect to the stacking direction - a feature that is not inherent to all other stacking patterns at the level of the molecular crystals.

Dynamical studies indicate that core movement quantified via vectors normal and coplanar to the cores is minimal in the nanosecond regime, a finding suggesting reduced spatial defects - a pivotal characteristic for charge transport applications.

Discotic tri-arm “super-molecules” with C16,4 side groups and TPB covalent linking are examined at the bulk molecular crystal level. A chiral stacking pattern of a linkage twist angle of 10° is found to be most preferable for all examined systems. In the case of C96- and C132-based tri-arm molecules, a detailed stacking pattern analysis is performed, showing that PAH segments adopt different stacking patterns compared to discotic single crystals. The compound stacking motifs inherit to tri-arm systems yield larger CTI values, indicating that the formed discotic triple helices can serve as an alternative charge transport system. Especially for C132 tri-arm systems, the “notorious” 90° stacking pattern is altogether avoided, suggesting potential applications of this extended PAH for organic electronic applications.

Furthermore, the overall effect of the side chain nanophase features on the structure and dynamics of tri-arm bulk systems is examined via an asymmetric substitution scheme that relies on leaving one of the three cores in its pristine form. A counterintuitive behavior is

manifested, showing that symmetrically substituted systems are more robust. The aforementioned findings suggest that the side chain nanophase is not only a means of solubilization, but a cohesive agent as well that minimizes core libration and stabilizes the supramolecular assembly.

Bearing in mind the intricate effects of soft, flexible nanophases on overall physicochemical properties of liquid-crystalline systems (e.g. odd/even or overall side chain length effects on transition temperatures and manifestation of different phases),[96] this very phenomenon should not be considered peculiar at all. Moreover, this stabilizing effect due to symmetric functionalization could ultimately be traced back to the depletion effect as observed in col-loid/polymer systems, with the cores of the liquid-crystal molecules playing the role of the colloidal particles and the aliphatic tails that of the added non-adsorbing polymers.[97]

Although the asymmetric substitution failed to yield a more stable candidate for bulk assembly, its utilization in the form of an interfacial system is a promising alternative application of tri-arm "super-molecules". In such a form, pristine discotic cores adopt near graphitic-like stacking patterns, capable of exhibiting viable charge transfer. Moreover, monolayers of asymmetrically substituted tri-arm systems can serve as exposed nanopatterned nanographene arrays with a plethora of applications.

In conclusion, an intriguing aspect pertinent to polyaromatic stacking is vividly elucidated through Figures 6 to 10: upon functionalization with flexible side chains, mesogens such as C96 and C132 adopt energetically favourable stacking patterns that hinder charge transfer mechanisms via low electronic couplings. The utilization of three-fold molecular linkers can be considered as a first step towards coercing discotic units into adopting stacking motifs capable of more efficient charge transport. Coupled to other modification methods, such as the interplay between different side chain types grafted on specific functionalization sites[45] and the utilization of polar groups,[95] this type of molecular alteration can be added to the arsenal of synthetic chemists towards the rational design of novel materials for organic electronics applications.

Acknowledgement

This research has been co-financed by the European Union (European Social Fund - ESF) and Greek national funds through the Operational Programme “Education and Lifelong Learning” of the National Strategic Reference Framework (NSRF) - Research Funding Programme: THALIS. Investing in knowledge society through the European social fund [grant number MIS 379436] and by the IKY Fellowships of Excellence for Postgraduate Studies in Greece - Siemens Programme [award number 11126/13a].

This work was also supported by computational resources granted by the Greek Research and Technology Network (GRNET) on the National HPC facility “ARIS” under the projects “Multiscale Simulations of Crystalline and Liquid-Crystalline Systems - MultiCLC”, “Hierarchical Modeling of Soft Matter - HMSM” and “Molecular Simulations of Membrane-based Systems - MSMS”.

The authors thank Prof. G. Floudas for fruitful discussions regarding discotic systems from an experimentalist’s point of view and Dr. K. Vanommeslaeghe for providing a standalone version of the CGenFF conversion program.

Supporting Information Available

A list of level of theory per molecule for DFT calculations and benchmarking material for reorganization energy and charge transfer integral calculations are given in the Supporting Information. Figures pertinent to dimer and trimer configurations based on *hexa*-methyl substituted C96 are also provided, along with MD trajectory snapshots relevant to Figure 11. Finally, for force field benchmarking purposes, theoretical X-ray diffraction spectra and columnar diffusion characteristics for the HBC-C16,4 molecular crystal are also included in the Supporting Information.

References

(1) Wu, J.; Pisula, W.; Müllen, K. Graphenes as Potential Material for Electronics. *Chem. Rev.* ***2007***, *107*, 718–747.

(2) Wöhrle, T.; Beardsworth, S. J.; Schilling, C.; Baro, A.; Giesselmann, F.; Laschat, S. Columnar propeller-like 1,3,5-triphenylbenzenes: the missing link of shape-persistent hekates. *Soft Matter* ***2016***, *12*, 3730–3736.

(3) Simpson, C. D.; Wu, J.; Watson, M. D.; Müllen, K. From graphite molecules to columnar superstructures - an exercise in nanoscience. *J. Mater. Chem.* ***2004***, *14*, 494–504.

(4) Brédas, J. L.; Calbert, J. P.; da Silva Filho, D. A.; Cornil, J. Organic semiconductors: A theoretical characterization of the basic parameters governing charge transport. *PNAS* ***2002***, *99*, 5804–5809.

(5) Wunderlich, K.; Grigoriadis, C.; Zardalidis, G.; Klapper, M.; Graf, R.; Butt, H.-J.; Müllen, K.; Floudas, G. Poly(ethylene glycol)-Functionalized Hexaphenylbenzenes as Unique Amphiphiles: Supramolecular Organization and Ion Conductivity. *Macromolecules* ***2014***, *47*, 5691–5702.

(6) Pipertzis, A.; Zardalidis, G.; Wunderlich, K.; Klapper, M.; Müllen, K.; Floudas, G. Ionic Conduction in Poly(ethylene glycol)-Functionalized Hexa-peri-hexabenzocoronene Amphiphiles. *Macromolecules* ***2017***, *50*, 1981–1990.

(7) Yen, H.-J. et al. Structurally Defined 3D Nanographene Assemblies via Bottom-Up Chemical Synthesis for Highly Efficient Lithium Storage. *Adv. Mater.* ***2016***, *28*, 10250– 10256.

(8) Lim, Y.; Lee, S.; Jang, H.; Yoo, J.; Ha, J.; Ju, H.; Hong, T.; Kim, W. New multi-phenylene polymer electrolyte containing hexabenzocoronene interior for PEMFC. *Int. J. Hydrogen Energy* ***2015***, *40*, 1316–1323.

(9) Wang, P.-I.; Pisula, W.; Müllen, K.; Liaw, D.-J. Structurally defined nanographene-containing conjugated polymers for high quality dispersions and optoelectronic applications. *Polym. Chem.* **2016**, *7*, 6211–6219.

(10) Gao, C.; Qiao, Z.; Shi, K.; Chen, S.; Li, Y.; Yu, G.; Li, X.; Wang, H. Hexa- peri -hexabenzocoronene and diketopyrrolopyrrole based D-A conjugated copolymers for organic field effect transistor and polymer solar cells. *Org. Electron.* **2016**, *38*, 245–255.

(11) Thompson, C. M.; McCandless, G. T.; Wijenayake, S. N.; Alfarawati, O.; Jahangiri, M.; Kokash, A.; Tran, Z.; Smaldone, R. A. Substituent Effects on the Gas Sorption and Selectivity Properties of Hexaphenylbenzene and Hexabenzocoronene Based Porous Polymers. *Macromolecules* **2014**, *47*, 8645–8652.

(12) Karunathilake, A. A. K.; Chang, J.; Thompson, C. M.; Nguyen, C. U.; Nguyen, D. Q.; Rajan, A.; Sridharan, A.; Vyakaranam, M.; Adegboyega, N.; Kim, S. J.; Smal-done, R. A. Hexaphenylbenzene and hexabenzocoronene-based porous polymers for the adsorption of volatile organic compounds. *RSC Adv.* **2016**, *6*, 65763–65769.

(13) Duran, H.; Hartmann-Azanza, B.; Steinhart, M.; Gehrig, D.; Laquai, F.; Feng, X.; Müllen, K.; Butt, H.-J.; Floudas, G. Arrays of Aligned Supramolecular Wires by Macroscopic Orientation of Columnar Discotic Mesophases. *ACS Nano* **2012**, *6*, 9359–9365.

(14) Zhang, R.; Ungar, G.; Zeng, X.; Shen, Z. Diverse configurations of columnar liquid crystals in cylindrical nano- and micropores. *Soft Matter* **2017**, *13*, 4122–4131.

(15) Yan, X.; Cui, X.; Li, L. Synthesis of Large, Stable Colloidal Graphene Quantum Dots with Tunable Size. *J. Am. Chem. Soc.* **2010**, *132*, 5944–5945.

(16) Zhu, S.; Wang, L.; Li, B.; Song, Y.; Zhao, X.; Zhang, G.; Zhang, S.; Lu, S.; Zhang, J.; Wang, H.; Sun, H.; Yang, B. Investigation of photoluminescence mechanism of graphene quantum dots and evaluation of their assembly into polymer dots. *Carbon* **2014**, *77*, 462–472.

(17) Yuan, B.; Sun, X.; Yan, J.; Xie, Z.; Chen, P.; Zhou, S. C96H30 tailored single-layer and single-crystalline graphene quantum dots. *Phys. Chem. Chem. Phys.* ***2016***, *18*, 25002–25009.

(18) Zhu, S.; Song, Y.; Wang, J.; Wan, H.; Zhang, Y.; Ning, Y.; Yang, B. Photoluminescence mechanism in graphene quantum dots: Quantum confinement effect and surface/edge state. *Nano Today* ***2017***, *13*, 10–14.

(19) Mackie, I. D.; DiLabio, G. A. Interactions in Large, Polyaromatic Hydrocarbon Dimers: Application of Density Functional Theory with Dispersion Corrections. *J. Phys. Chem. A* ***2008***, *112*, 10968–10976.

(20) Zhao, Y.; Truhlar, D. G. A Prototype for Graphene Material Simulation: Structures and Interaction Potentials of Coronene Dimers. *J. Phys. Chem. C* ***2008***, *112*, 4061– 4067.

(21) Nagai, H.; Nakano, M.; Yoneda, K.; Fukui, H.; Minami, T.; Bonness, S.; Kishi, R.; Takahashi, H.; Kubo, T.; Kamada, K.; Ohta, K.; Champagne, B.; Botek, E. Theoretical study on third-order nonlinear optical properties in hexagonal graphene nanoflakes: Edge shape effect. *Chem. Phys. Lett.* ***2009***, *477*, 355–359.

(22) Antony, J.; Alameddine, B.; Jenny, T. A.; Grimme, S. Theoretical Study of the Stacking Behavior of Selected Polycondensed Aromatic Hydrocarbons with Various Symmetries. *J. Phys. Chem. A* ***2013***, *117*, 616–625.

(23) Li, J.; Liu, Y.; Qian, Y.; Li, L.; Xie, L.; Shang, J.; Yu, T.; Yi, M.; Huang, W. Describing curved–planar ÏĂ-ÏĂ interactions: modeled by corannulene, pyrene and coronene. *Phys. Chem. Chem. Phys.* ***2013***, *15*, 12694.

(24) Rivero, P.; Jiménez-Hoyos, C. A.; Scuseria, G. E. Entanglement and Polyradical Character of Polycyclic Aromatic Hydrocarbons Predicted by Projected Hartree-Fock Theory. *J. Phys. Chem. B* ***2013***, *117*, 12750–12758.

(25) Hu, W.; Lin, L.; Yang, C.; Yang, J. Electronic structure and aromaticity of large-scale hexagonal graphene nanoflakes. *J. Chem. Phys.* **2014**, *141*, 214704.

(26) Sanyal, S.; Manna, A. K.; Pati, S. K. Functional Corannulene: Diverse Structures, Enhanced Charge Transport, and Tunable Optoelectronic Properties. *ChemPhysChem* **2014**, *15*, 885–893.

(27) Tsetseris, L. Hydrogen- and oxygen-related effects in phthalocyanine crystals: formation of carrier traps and a change in the magnetic state. *Phys. Chem. Chem. Phys.* **2014**, *16*, 3317–3322.

(28) Tsetseris, L. Functionalization of Nanographenes: Metallic and Insulating Hexabenzocoronene Derivatives. *J. Phys. Chem. C* **2014**, *118*, 1347–1352.

(29) Karadakov, P. B. Do large polycyclic aromatic hydrocarbons and graphene bend? How popular theoretical methods complicate finding the answer to this question. *Chem. Phys. Lett.* **2016**, *646*, 190–196.

(30) Kirkpatrick, J.; Marcon, V.; Kremer, K.; Nelson, J.; Andrienko, D. Columnar mesophases of hexabenzocoronene derivatives. II. Charge carrier mobility. *J. Chem. Phys.* **2008**, *129*, 094506.

(31) Troisi, A.; Cheung, D. L.; Andrienko, D. Charge Transport in Semiconductors with Multiscale Conformational Dynamics. *Phys. Rev. Lett.* **2009**, *102*, 116602.

(32) Vehoff, T.; Baumeier, B.; Troisi, A.; Andrienko, D. Charge Transport in Organic Crystals: Role of Disorder and Topological Connectivity. *J. Am. Chem. Soc.* **2010**, *132*, 11702–11708.

(33) Navarro, A.; Fernández-Liencres, M. P.; Garcia, G.; Granadino-Roldán, J. M.; Fernández-Gómez, M. A DFT approach to the charge transport related properties

in columnar stacked π-conjugated N-heterocycle cores including electron donor and acceptor units. *Phys. Chem. Chem. Phys.* ***2015***, *17*, 605–618.

(34) Cinacchi, G.; Colle, R.; Tani, A. Atomistic Molecular Dynamics Simulation of Hexakis(pentyloxy)triphenylene: Structure and Translational Dynamics of Its Columnar State. *J. Phys. Chem. B* ***2004***, *108*, 7969–7977.

(35) Cinacchi, G. Atomistic Molecular Dynamics Simulation of Benzene as a Solute in a Columnar Discotic Liquid Crystal. *J. Phys. Chem. B* ***2005***, *109*, 8125–8131.

(36) Andrienko, D.; Marcon, V.; Kremer, K. Atomistic simulation of structure and dynamics of columnar phases of hexabenzocoronene derivatives. *J. Chem. Phys.* ***2006***, *125*, 124902.

(37) Muccioli, L.; Berardi, R.; Orlandi, S.; Ricci, M.; Zannoni, C. Molecular properties and stacking of 1-substituted hexaalkoxy triphenylenes. *Theor. Chem. Acc.* ***2007***, *117*, 1085–1092.

(38) Marcon, V.; Vehoff, T.; Kirkpatrick, J.; Jeong, C.; Yoon, D. Y.; Kremer, K.; An-drienko, D. Columnar mesophases of hexabenzocoronene derivatives. I. Phase transitions. *J. Chem. Phys.* ***2008***, *129*, 094505.

(39) Ziogos, O. G.; Theodorou, D. N. Molecular dynamics simulations of alkyl substituted nanographene crystals. *Mol. Phys.* ***2015***, *113*, 2776–2790.

(40) Kirkpatrick, J.; Marcon, V.; Nelson, J.; Kremer, K.; Andrienko, D. Charge Mobility of Discotic Mesophases: A Multiscale Quantum and Classical Study. *Phys. Rev. Lett.* ***2007***, *98*, 227402.

(41) Kirkpatrick, J.; Marcon, V.; Kremer, K.; Nelson, J.; Andrienko, D. Charge transport parameters of HBC at different temperatures. *Phys. Status Solidi B* ***2008***, *245*, 835– 838.

(42) Andrienko, D.; Kirkpatrick, J.; Marcon, V.; Nelson, J.; Kremer, K. Structure-charge mobility relation for hexabenzocoronene derivatives. *Phys. Status Solidi B* ***2008***, *245*, 830–834.

(43) Cinacchi, G.; Colle, R.; Parruccini, P.; Tani, A. Structural, electronic, and optical properties of a prototype columnar discotic liquid crystal. *J. Chem. Phys.* ***2008***, *129*, 174708.

(44) Marcon, V.; Breiby, D. W.; Pisula, W.; Dahl, J.; Kirkpatrick, J.; Patwardhan, S.; Grozema, F.; Andrienko, D. Understanding Structure-Mobility Relations for Perylene Tetracarboxydiimide Derivatives. *J. Am. Chem. Soc.* ***2009***, *131*, 11426–11432.

(45) Feng, X.; Marcon, V.; Pisula, W.; Hansen, M. R.; Kirkpatrick, J.; Grozema, F.; An-drienko, D.; Kremer, K.; Müllen, K. Towards high charge-carrier mobilities by rational design of the shape and periphery of discotics. *Nat. Mater.* ***2009***, *8*, 421–426.

(46) Idé, J.; Méreau, R.; Ducasse, L.; Castet, F.; Bock, H.; Olivier, Y.; Cornil, J.; Beljonne, D.; D'Avino, G.; Roscioni, O. M.; Muccioli, L.; Zannoni, C. Charge Dissociation at Interfaces between Discotic Liquid Crystals: The Surprising Role of Column Mismatch. *J. Am. Chem. Soc.* ***2014***, *136*, 2911–2920.

(47) van de Craats, A. M.; Warman, J. M. The Core-Size Effect on the Mobility of Charge in Discotic Liquid Crystalline Materials. *Adv. Mater.* ***2001***, *13*, 130–133.

(48) Debije, M. G.; Piris, J.; de Haas, M. P.; Warman, J. M.; Tomović, Ž.; Simpson, C. D.; Watson, M. D.; Müllen, K. The Optical and Charge Transport Properties of Discotic Materials with Large Aromatic Hydrocarbon Cores. *J. Am. Chem. Soc.* ***2004***, *126*, 4641–4645.

(49) Fischbach, I.; Pakula, T.; Minkin, P.; Fechtenkötter, A.; Müllen, K.; Spiess, H. W.; Saalwächter, K. Structure and Dynamics in Columnar Discotic Materials: A Combined

X-ray and Solid-State NMR Study of Hexabenzocoronene Derivatives. *J. Phys. Chem. B* ***2002***, *106*, 6408–6418.

(50) van de Craats, A. M.; Warman, J. M.; Fechtenkötter, A.; Brand, J. D.; Harbison, M. A.; Müllen, K. Record Charge Carrier Mobility in a Room-Temperature Discotic Liquid-Crystalline Derivative of Hexabenzocoronene. *Adv. Mater.* ***1999***, *11*, 1469–1472.

(51) Pisula, W.; Menon, A.; Stepputat, M.; Lieberwirth, I.; Kolb, U.; Tracz, A.; Sirring-haus, H.; Pakula, T.; Müllen, K. A Zone-Casting Technique for Device Fabrication of Field-Effect Transistors Based on Discotic Hexa-peri-hexabenzocoronene. *Adv. Mater.* ***2005***, *17*, 684–689.

(52) Wu, J.; Baumgarten, M.; Debije, M. G.; Warman, J. M.; Müllen, K. Arylamine-Substituted Hexa-peri-hexabenzocoronenes: Facile Synthesis and Their Potential Applications as "Coaxial" Hole-Transport Materials. *Angew. Chem.* ***2004***, *116*, 5445–5449.

(53) Grimsdale, A. C.; Wu, J.; Müllen, K. New carbon-rich materials for electronics, lithium battery, and hydrogen storage applications. *Chem. Commun.* ***2005***, 2197–2204.

(54) Wu, J.; Watson, M. D.; Tchebotareva, N.; Wang, Z.; Müllen, K. Oligomers of Hexa-peri-hexabenzocoronenes as "Super-oligophenylenes": Synthesis, Electronic Properties, and Self-assembly. *J. Org. Chem.* ***2004***, *69*, 8194–8204.

(55) Goddard, R.; Haenel, M. W.; Herndon, W. C.; Krüger, C.; Zander, M. Crystallization of Large Planar Polycyclic Aromatic Hydrocarbons: The Molecular and Crystal Structures of Hexabenzo[bc,ef,hi,kl,no,qr]coronene and Benzo[1,2,3-bc:4,5,6-b'c']dicoronene. *J. Am. Chem. Soc.* ***1995***, *117*, 30–41.

(56) Tomović, Ž.; Watson, M. D.; Müllen, K. Superphenalene-Based Columnar Liquid Crystals. *Angew. Chem. Int. Ed.* ***2004***, *43*, 755–758.

(57) Samorí, P.; Severin, N.; Simpson, C. D.; Müllen, K.; Rabe, J. P. Epitaxial Composite Layers of Electron Donors and Acceptors from Very Large Polycyclic Aromatic Hydrocarbons. *J. Am. Chem. Soc.* ***2002***, *124*, 9454–9457.

(58) Friedlein, R.; Crispin, X.; Simpson, C. D.; Watson, M. D.; Jäckel, F.; Osikowicz, W.; Marciniak, S.; de Jong, M. P.; Samorí, P.; Jönsson, S. K. M.; Fahlman, M.; Müllen, K.; Rabe, J. P.; Salaneck, W. R. Electronic structure of highly ordered films of self-assembled graphitic nanocolumns. *Phys. Rev. B* ***2003***, *68*, 195414.

(59) Fechtenkötter, A.; Tchebotareva, N.; Watson, M.; Müllen, K. Discotic liquid crystalline hexabenzocoronenes carrying chiral and racemic branched alkyl chains: supramolecular engineering and improved synthetic methods. *Tetrahedron* ***2001***, *57*, 3769–3783.

(60) Pisula, W.; Tomović, Ž.; Simpson, C.; Kastler, M.; Pakula, T.; Müllen, K. Relationship between Core Size, Side Chain Length, and the Supramolecular Organization of Polycyclic Aromatic Hydrocarbons. *Chem. Mater.* ***2005***, *17*, 4296–4303.

(61) Boden, N.; Bushby, R. J.; Cammidge, A. N.; El-Mansoury, A.; Martin, P. S.; Lu, Z. The creation of long-lasting glassy columnar discotic liquid crystals using 'dimeric' discogens. *J. Mater. Chem.* ***1999***, *9*, 1391–1402.

(62) Aytun, T.; Santos, P. J.; Bruns, C. J.; Huang, D.; Koltonow, A. R.; de la Cruz, M. O.; Stupp, S. I. Self-Assembling Tripodal Small-Molecule Donors for Bulk Heterojunction Solar Cells. *J. Phys. Chem. C* ***2016***, *120*, 3602–3611.

(63) Zhang, Y.; Hanifi, D. A.; Fernández-Liencres, M. P.; Klivansky, L. M.; Ma, B.; Navarro, A.; Liu, Y. Understanding Electron Transport in Disk-Shaped Triphenylene-Tris(naphthaleneimidazole)s through Structural Modification and Theoretical Investigation. *ACS Appl. Mater. Interfaces* ***2017***, *9*, 20010–20019.

(64) Nakano, T.; Morisaki, Y.; Chujo, Y. Synthesis of hexabenzocoronene-layered compounds. *Tetrahedron Lett.* ***2015***, *56*, 2086–2090.

(65) Grimsdale, A. C.; Müllen, K. The Chemistry of Organic Nanomaterials. *Angew. Chem. Int. Ed.* ***2005***, *44*, 5592–5629.

(66) Türp, D.; Nguyen, T.-T.-T.; Baumgarten, M.; Müllen, K. Uniquely versatile: nano-site defined materials based on polyphenylene dendrimers. *New J. Chem.* ***2012***, *36*, 282–298.

(67) Dogru, M.; Bein, T. On the road towards electroactive covalent organic frameworks. *Chem. Commun.* ***2014***, *50*, 5531–5546.

(68) Bai, Y.-F.; Chen, L.-Q.; Hu, P.; Luo, K.-J.; Yu, W.-H.; Ni, H.-L.; Zhao, K.-Q.; Wang, B.-Q. Synthesis and characterisation of 3-armed dendritic molecules with triph-enylbenzene or triphenyltriazine as core and triphenylene derivative as shells. *Liq. Cryst.* ***2015***, *42*, 1591–1600.

(69) Wöhrle, T.; Wurzbach, I.; Kirres, J.; Kostidou, A.; Kapernaum, N.; Litterscheidt, J.; Haenle, J. C.; Staffeld, P.; Baro, A.; Giesselmann, F.; Laschat, S. Discotic Liquid Crystals. *Chem. Rev.* ***2016***, *116*, 1139–1241.

(70) Lee, C.; Yang, W.; Parr, R. G. Development of the Colle-Salvetti correlation-energy formula into a functional of the electron density. *Phys. Rev. B* ***1988***, *37*, 785–789.

(71) Becke, A. D. Density-functional thermochemistry. III. The role of exact exchange. *J. Chem. Phys.* ***1993***, *98*, 5648–5652.

(72) Grimme, S.; Antony, J.; Ehrlich, S.; Krieg, H. A consistent and accurate ab initio parametrization of density functional dispersion correction (DFT-D) for the 94 elements H-Pu. *J. Chem. Phys.* ***2010***, *132*, 154104.

(73) Deng, W.-Q.; Goddard, W. A. Predictions of Hole Mobilities in Oligoacene Organic Semiconductors from Quantum Mechanical Calculations. *J. Phys. Chem. B* ***2004***, *108*, 8614–8621.

(74) Hutchison, G. R.; Ratner, M. A.; Marks, T. J. Hopping Transport in Conductive Heterocyclic Oligomers: Reorganization Energies and Substituent Effects. *J. Am. Chem. Soc.* **2005**, *127*, 2339–2350.

(75) Valeev, E. F.; Coropceanu, V.; da Silva Filho, D. A.; Salman, S.; Brédas, J.-L. Effect of Electronic Polarization on Charge-Transport Parameters in Molecular Organic Semiconductors. *J. Am. Chem. Soc.* **2006**, *128*, 9882–9886.

(76) Valiev, M.; Bylaska, E.; Govind, N.; Kowalski, K.; Straatsma, T.; Dam, H. V.; Wang, D.; Nieplocha, J.; Apra, E.; Windus, T.; de Jong, W. NWChem: A comprehensive and scalable open-source solution for large scale molecular simulations. *Comput. Phys. Commun.* **2010**, *181*, 1477–1489.

(77) Vanommeslaeghe, K.; Hatcher, E.; Acharya, C.; Kundu, S.; Zhong, S.; Shim, J.; Dar-ian, E.; Guvench, O.; Lopes, P.; Vorobyov, I.; Mackerell, A. D. CHARMM general force field: A force field for drug-like molecules compatible with the CHARMM all-atom additive biological force fields. *J. Comput. Chem.* **2010**, *31*, 671–690.

(78) Yu, W.; He, X.; Vanommeslaeghe, K.; MacKerell, A. D. Extension of the CHARMM general force field to sulfonyl-containing compounds and its utility in biomolecular simulations. *Journal of Computational Chemistry* **2012**, *33*, 2451–2468.

(79) Wang, J.; Wolf, R. M.; Caldwell, J. W.; Kollman, P. A.; Case, D. A. Development and testing of a general amber force field. *J. Comput. Chem.* **2004**, *25*, 1157–1174.

(80) Jorgensen, W. L.; Madura, J. D.; Swenson, C. J. Optimized intermolecular potential functions for liquid hydrocarbons. *J. Am. Chem. Soc.* **1984**, *106*, 6638–6646.

(81) Jorgensen, W. L.; Severance, D. L. Aromatic-aromatic interactions: free energy profiles for the benzene dimer in water, chloroform, and liquid benzene. *J. Am. Chem. Soc.* **1990**, *112*, 4768–4774.

(82) Oostenbrink, C.; Villa, A.; Mark, A. E.; Gunsteren, W. F. V. A biomolecular force field based on the free enthalpy of hydration and solvation: The GROMOS force-field parameter sets 53A5 and 53A6. *J. Comput. Chem.* ***2004***, *25*, 1656–1676.

(83) Martyna, G. J.; Tobias, D. J.; Klein, M. L. Constant pressure molecular dynamics algorithms. *J. Chem. Phys.* ***1994***, *101*, 4177–4189.

(84) Hockney, R.; Eastwood, J. *Computer Simulation Using Particles*; Taylor & Francis, 1988.

(85) Isele-Holder, R. E.; Mitchell, W.; Ismail, A. E. Development and application of a particle-particle particle-mesh Ewald method for dispersion interactions. *J. Chem. Phys.* ***2012***, *137*, 174107.

(86) Plimpton, S. Fast Parallel Algorithms for Short-Range Molecular Dynamics. *J. Comput. Phys.* ***1995***, *117*, 1–19.

(87) Theodorou, D. N.; Suter, U. W. Detailed molecular structure of a vinyl polymer glass. *Macromolecules* ***1985***, *18*, 1467–1478.

(88) Thomas, L. L.; Christakis, T. J.; Jorgensen, W. L. Conformation of Alkanes in the Gas Phase and Pure Liquids. *J. Phys. Chem. B* ***2006***, *110*, 21198–21204.

(89) Mayo, S. L.; Olafson, B. D.; Goddard, W. A. DREIDING: a generic force field for molecular simulations. *J. Phys. Chem.* ***1990***, *94*, 8897–8909.

(90) Rappe, A. K.; Casewit, C. J.; Colwell, K. S.; Goddard, W. A.; Skiff, W. M. UFF, a full periodic table force field for molecular mechanics and molecular dynamics simulations. *J. Am. Chem. Soc.* ***1992***, *114*, 10024–10035.

(91) Adamo, C.; Barone, V. Toward reliable density functional methods without adjustable parameters: The PBE0 model. *J. Chem. Phys.* ***1999***, *110*, 6158–6170.

(92) Yang, B. et al. The Origin of the Improved Efficiency and Stability of Triphenylamine-Substituted Anthracene Derivatives for OLEDs: A Theoretical Investigation. *ChemPhysChem* ***2008***, *9*, 2601–2609.

(93) Lee, J.-K.; Kim, J.-G.; Hembram, K. P. S. S.; Kim, Y.-I.; Min, B.-K.; Park, Y.; Lee, J.-K.; Moon, D. J.; Lee, W.; Lee, S.-G.; John, P. The Nature of Metastable AA' Graphite: Low Dimensional Nano- and Single-Crystalline Forms. *Sci. Rep.* ***2016***, *6*, 39624.

(94) Brown, S. P.; Schnell, I.; Brand, J. D.; Müllen, K.; Spiess, H. W. An Investigation of π-π Packing in a Columnar Hexabenzocoronene by Fast Magic-Angle Spinning and Double-Quantum1H Solid-State NMR Spectroscopy. *J. Am. Chem. Soc.* ***1999***, *121*, 6712–6718.

(95) Grigoriadis, C.; Haase, N.; Butt, H.-J.; Müllen, K.; Floudas, G. Negative Thermal Expansion in Discotic Liquid Crystals of Nanographenes. *Adv. Mater.* ***2010***, *22*, 1403– 1406.

(96) Demus, D., Goodby, J., Gray, G. W., Spiess, H.-W., Vill, V., Eds. *Handbook of Liquid Crystals*; Wiley-VCH Verlag GmbH, 1998.

(97) Asakura, S.; Oosawa, F. Interaction between particles suspended in solutions of macro-molecules. *J. Polym. Sci.* ***1958***, *33*, 183–192.

Graphical TOC Entry